CHALMERS
UNIVERSITY OF TECHNOLOGY

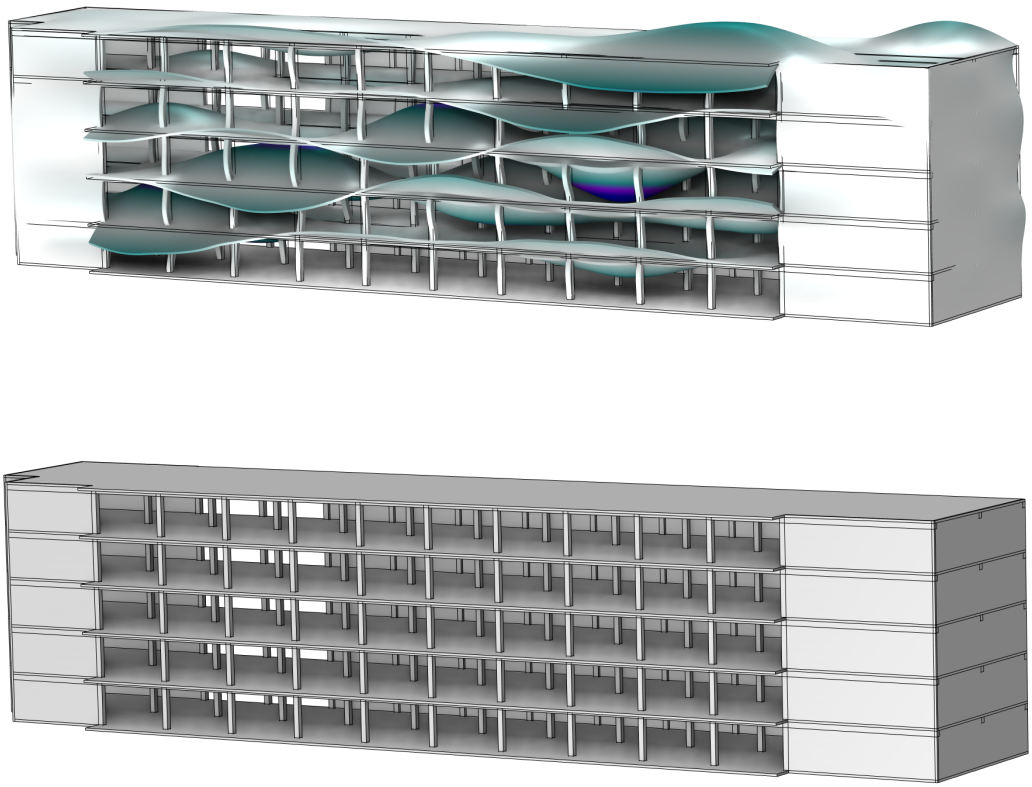

Low-Frequency Vibrational Behaviour in Concrete Structures

Exploring Structural Reverberation Time and Distance-Based Attenuation Trends Across Building Floors

Master's thesis in Master Programme Sound and Vibrations

Mårten Muregård and Jonna Parkkonen

DEPARTMENT OF SOME SUBJECT OR TECHNOLOGY
CHALMERS UNIVERSITY OF TECHNOLOGY
Gothenburg, Sweden 2025
www.chalmers.se

Master's thesis 2025

Low-Frequency Vibrational Behaviour in Concrete Structures

Exploring Structural Reverberation Time and Distance-Based Attenuation Trends Across Building Floors

MÅRTEN MUREGÅRD
JONNA PARKKONEN

CHALMERS
UNIVERSITY OF TECHNOLOGY

Department of Civil Engineering and Architecture
Division of Technical Acoustics
Chalmers University of Technology
Gothenburg, Sweden 2025

Low-Frequency Vibrational Behaviour in Concrete Structures
Exploring Structural Reverberation Time and Distance-Based Attenuation Trends Across Building Floors
MÅRTEN MUREGÅRD and JONNA PARKKONEN

© MÅRTEN MUREGÅRD & JONNA PARKKONEN, 2025.

Supervisor: Mange Skålevik, Brekke & Strand
Examiner: Jens Forssén

Master's Thesis 2025
Department of Civil Engineering and Architecture
Division of Technical Acoustics
Chalmers University of Technology
SE-412 96 Gothenburg
Telephone +46 31 772 1000

Cover: Comsol model and one of its mode shapes.

Typeset in LaTeX
Printed by Chalmers Reproservice
Gothenburg, Sweden 2025

Low-Frequency Vibrational Behaviour in Concrete Structures
MÅRTEN MUREGÅRD
JONNA PARKKONEN
Department of Civil Engineering and Architecture
Chalmers University of Technology

Abstract

This thesis investigates low-frequency structure-borne sound propagation in concrete floor slabs across multiple floors of a building. The study aims to assess whether a relationship exists between reverberation time, distance-dependent vibration level decay, and group velocity. Both in-situ measurements and numerical simulations using Comsol Multiphysics were conducted to analyse structural vibrational behaviour and estimate parameters such as propagation velocity, reverberation time, and attenuation per distance (dB/m) in the 50–160 Hz third-octave band range.

The structural impulse responses were post-processed through backward integration and time-delay estimation techniques, allowing for comparison between simulated and real building conditions. Five analytical propagation models combining geometrical spreading and damping were fitted to the data using Matlab functions. The results from both simulations and measurements suggest that no consistent or global link could be established for the reverberation time (T_{60}), and therefore no clear proportional relationship was found between T_{60} and the vibrational level decay over distance (L_a). However, some tendencies toward a proportional relationship between L_a per distance and the effective group velocity c_{eff} were observed. Notably, the velocity trends diverged between simulation and measurement, indicating potential differences in wave type dominance over distance for the measured data and the simulated results.

The findings reveal the limitations of modeling large, complex structures due to computational constraints and emphasise the importance of local geometry and boundary conditions in structural acoustic behaviour. Although a complete predictive model could not be established, this work provides a framework for assessing energy-based decay behaviour in solid structures. It proposes directions for future development of building-scale low-frequency vibration prediction models.

Keywords: vibrations, structures, modal-analysis, Matlab, Comsol Multi-Physics, deconvolution, concrete, estimated vibrational propagation velocity.

AI Involvement and Transparency Declaration

This master's thesis involved various artificial intelligence tools to enhance the research and writing process throughout the work. ChatGPT-4o was employed for code debugging, generating code in Latex, and literature searches as well for Comsol Multiphysics navigation within the software. Additionally, Grammarly and ChatGPT were used to ensure proper grammar, spelling and sentence structure throughout the thesis.

Acknowledgements

We thank our supervisor Magne Skålevik, senior acoustician at Brekke & Strand for proposing this master's thesis and guiding and helping us throughout the project with his long standing professional expertise in the area.

We would like to express our gratitude to our examiner Jens Forssén, professor at the Division of Applied Acoustics at Chalmers for guidance and help with all things related to our project.

Also thanks to Wolfgang Kropp, full professor at the Division of Applied Acoustics at Chalmers for allotting time for our questions, supporting and guiding us throughout this project.

Fatemeh Dashti, PhD student at the Division of Applied Acoustics also deserves thanks from us for helping us with our pilot measurement setup.

We also thank Krister Larsson, Research Associates at the Division of Applied Acoustics, for helping us with our pilot measurement setup.

Mårten Muregård & Jonna Parkkonen, Gothenburg, May 2025

List of Acronyms

Below is the list of acronyms that have been used throughout this thesis, listed in alphabetical order:

Acronym	**Definition**
Comsol	Comsol Multiphysics (simulation software)
dB/m	Decibel level reduction per meter of propagation
FFT	Fast Fourier Transform
FRF	Frequency Response Function
IFFT	Inverse Fast Fourier Transform
L_a	Vibration level based on acceleration, expressed in dB
LTI	Linear Time-Invariant
MDOF	Multiple Degrees of Freedom
SNR	Signal-to-Noise Ratio
T_{60}	Reverberation time

Nomenclature

Below is the nomenclature of symbols, indices, parameters, and variables used throughout this thesis. Symbols are described as they appear in equations or Figures, ordered by type.

Indices

$\mathbf{x}_0$	Excitation point (source location), defined in the global coordinate system, set to $\mathbf{x}_0 = (0, 0, 0)$
$\mathbf{x}_r$	Measurement point (receiver location), defined as $\mathbf{x}_r = (x_r, y_r, z_r)$ in the global coordinate system

Parameters

k	wave number (1/m)
T_s	sampling period (s)
Δt	Time delay between excitation and measurement (s)
t_c	Center time based on energy decay curve (s)
η	Material loss factor (-)
R^2	Coefficient of determination (-)
N_m	Number of modes (–)
N	Spreading coefficient in analytical attenuation (e.g. 10 for cylindrical and 20 for spherical) (–)
a	Acceleration (m/s^2)
c_0	Velocity in air (m/s)
c_b	Bending wave velocity (m/s)
c_g	Group velocity (m/s)
$c_{\text{g,eff}}$	Effective group velocity (m/s)
r	Distance from excitation source to receiver (m)
ρ	Material density (kg/m^3)

λ_B	Wavelength of bending waves (m)
$ParameterA$	Constant offset in analytical level decay model (dB)
$ParameterB$	Geometrical spreading coefficient (–), equivalent to N
$ParameterC$	Damping coefficient (-)
B	Bending stiffness (Nm^2)
D	Longitudinal stiffness (Nm)
B_{plates}	Bending stiffness (Nm^2)
m'	Mass per unit length or area (kg/m or kg/m^2)
ν	Poisson's ratio (–)
W	Radiated power (W)

Variables

f	Frequency (Hz)
Δt	Time delay between excitation point $\mathbf{x}_0$ and measurement point $\mathbf{x}_r$ (s)
t_c	Time delay between source and receiver (s)
L_a	Vibration level (dB)
ΔL	Change in vibration level with distance (dB)
$\Phi_n(x)$	Mode shape of the n-th eigenmode at position x (–)
ω_n	Angular eigenfrequency of the n-th mode (rad/s)
ω_0	Natural angular frequency (rad/s)
ω	Angular frequency (rad/s)
$H(x_r, \omega)$	Frequency response function giving acceleration at x_r per unit excitation force, obtained by modal superposition over all modes
$H(f)$	Frequency response function (– or complex)
$h(t)$	Impulse response (–)
E_{loss}	Energy lost per cycle (Joule)
$E_{\text{reversible}}$	Reversible (stored) energy (Joule)

Contents

List of Figures

List of Tables

1
Introduction

Improved understanding of low-frequency structure-borne vibration transmission in the range of 20 to 200 Hz is needed for both the design of new buildings and the assessment of existing ones, particularly in terms of noise radiation from low-frequency sources such as traffic noise. Low-frequency airborne noise has been proven to create an increase in risk of disturbance and sleep disruption [1]. Structural vibrations can also affect occupants, as they may result in both perceptible vibrations and low-frequency airborne noise radiation. Understanding how structural vibrations propagate through buildings is not only important for engineering purposes but also for the important reason of assessing potential impacts on human health and comfort. According to ISO 2631-1:1997, exposure to whole-body vibrations from structural vibrations and sound in buildings can negatively affect well-being and quality of life [2].

This thesis will investigate whether the structural reverberation time can be used to predict the vibrational level decay over distance, and whether a proportional relationship exists between the reverberation time and the vibrational level decay across distance, denoted by L_a. Here, L_a refers to the decay of vibration levels inside the structure, measured as acceleration level in dB. The goal is to determine if this relationship can be developed into an energy-based model — a model that could potentially be used as a prediction tool for structure-borne sound in large, complex buildings, accounting for both vertical, horizontal, and diagonal distances. However, this approach is grounded in the theory of airborne sound propagation, as outlined by Barron [3].

In this report, vibrations refer to mechanical oscillations in structural elements (measured and calculated as acceleration). Noise denotes airborne sound. Structure-borne sound refers to airborne sound that originates from vibrating structural elements. These terms are used distinctly throughout the thesis for clarity.

1.1 Background

Buildings that are built today can be combinations of different facilities, such as stores and residential environments. This creates a demand for the acoustical environment and the dividing elements between separating rooms. Current regulations and ISO standards only address directly adjoining elements, specifically room-to-room configurations separated by one wall. There is a need to explore a potential

prediction model for larger systems that cover entire buildings.

In buildings with mixed facility use, strong excitation forces can induce structure-borne vibrations that radiate as airborne noise, which easily transmits between rooms. The currently given directions from ISO standards and regulations limit how close you can place a room with continuously emitting sound sources, such as gyms and music rooms [4]. This new method might make the standard more nuanced, allowing the planning and design stage to generate more solutions for the building layout.

This thesis builds on energy-based approaches used in room acoustics to evaluate changes in reverberation time, as described in Auditorium Acoustics and Architectural Design [3]. In traditional room acoustics, reflected sound is often considered uniformly distributed within a space. However, as illustrated in Figure 1.1, the reflected sound level decreases with increasing distance from the source. This results in a linear decay of the sound level, even though the reverberation time remains the same throughout the room. The key observation is that reverberation starts at different times depending on the receiver's position, allowing for estimation of the level decay per second. If the sound velocity is known, this time-based decay can be converted into a decay per distance, expressed in dB per meter [3].

While this principle has been well established for airborne sound in gaseous media, its application to solid structures remains limited. An earlier study by Cheng Jiali investigated the relationship between structural reverberation time and level decay on a single concrete floor. The study suggested future work should involve multi-floor systems in three dimensions, enabling analysis in more complex geometries [5].

In this context, the goal of the current thesis is to examine whether the concept of energy-based level decay can be applied to structure-borne vibrations and the resulting airborne noise. More specifically, it investigates whether the decay of vibrational levels in a structure, as measured by acceleration, can be predicted using the structural reverberation time. The broader aim is to explore whether this relationship can serve the basis for a predictive model of structure-borne sound in large buildings.

To summarise, this thesis investigates whether the decay of vibrational energy in concrete structures follows a consistent, linearly decaying trend with distance from the excitation point. The aim is to determine whether all measurement points conform to this trend, indicating the presence of a global reverberation time, a single parameter that describes the energy decay across the entire structure. If such a relationship can be established, the reverberation time could serve as a predictive tool for structure-borne sound propagation in complex building geometries.

1.2 Aim & Research Questions

The aim of this thesis is to investigate the bending wave behaviour in concrete floor slabs across multiple floors of a building, using in-situ measurements and Comsol-

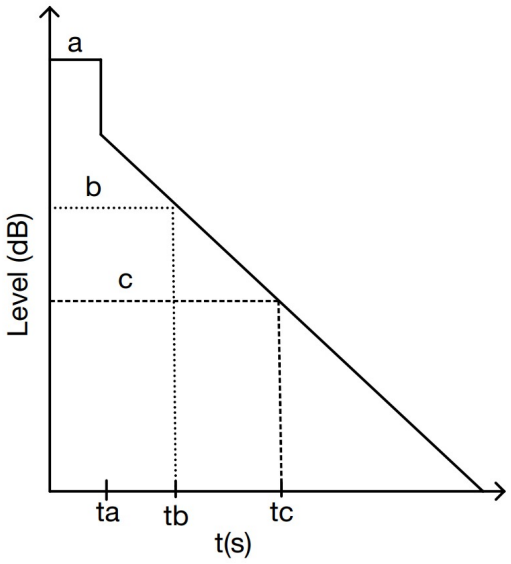

Figure 1.1: Impulse curves are shown for three different distances: the closest one is a, followed by b, and c from the source, where the slope represents the diffuse field after t_a [3, p. 464].

based numerical simulations.

Below is a list of the research questions that this thesis aims to answer.

- Is it possible to find a connection between the time difference of the reverberant field, Δt, and the distance d, between a receiver point and a driving point? Is the velocity $c_{\text{g,eff}} = \frac{d}{\Delta t}$?
- Is there a proportionality between the ratio of vibration level and distance, $\frac{\Delta L_a}{d}$, and the reverberation time?
- Is there a global structural reverberation time, or does it vary with location or transmission path?
- Is there a way to identify and measure the time delays Δt at different distances from the source?
- To what extent can a representative modal response, based on mode shapes and modal superposition, be modelled and simulated to accurately represent the dynamic behaviour of a real building using Comsol?

1.3 Delimitation

Delimitations for the thesis can be seen itemised below.

- High-frequency predictions of structure-borne sound are not included in this report. The focus will be on frequencies up to approximately 160 Hz.
- The topic of air transmission in structures will not be addressed.
- Only concrete structures are examined, with a focus on specific types of junctions. Cross-laminated timber will not be included as a structural system in

this investigation. However, it is noteworthy due to its increasing application in new developments, making it a topic of interest for future research.
- Delimitation in Comsol involves defining non-deformed cross-sections.
- Existential questions about the human condition will not be explored, even if they arise during the process of writing this master's thesis.

1.4 Division of Work

All work in this thesis has been carried out jointly by the authors. The workload has been shared equally between them throughout the whole process.

2
Theory

Structural vibrations involve complex physical phenomena and multiple interacting mechanisms. In this thesis, vibrations refer specifically to mechanical oscillations in building elements.

This chapter presents the theoretical background for evaluating how structural vibrations propagate in complex buildings. It will focus on how vibrations propagate in three dimensions using the finite element method, particularly for beams and plates.

The process from initial excitation to airborne noise radiation is also outlined to understand how structural vibrations can lead to airborne noise within a building.

2.1 Reverberation Time

The reverberation time T_{60} is an acoustical parameter that describes the duration required for the energy of a sound or vibration to decrease by 60 dB after the excitation source has stopped. Note that the reverberation time is expressed in seconds and can be evaluated based on a smaller dynamic range than 60 dB and extrapolated to a decay time of 60 dB [6].

2.2 The Effective Group velocity

For impulse responses, a so-called effective velocity can be calculated when both the level decay per meter and the reverberation time, T_{60}, are known. Equation 2.1 expresses the level decay over time:

$$\frac{\partial L}{\partial t} = \frac{-60}{T_{60}} \tag{2.1}$$

Equation 2.2 represents the level decay over distance r, where r is the distance from the source to the measurement point:

$$\frac{\partial L}{\partial r} \tag{2.2}$$

By combining these two expressions, an effective group velocity describing wave propagation in the reverberant field can be derived. This relationship was originally formulated in a master's thesis by Cheng [5, pp. 11–12]:

$$\frac{\partial L/\partial t}{\partial L/\partial r} = c_{\mathrm{g,eff}} \tag{2.3}$$

2.3 Behaviour of Wave Propagation in Finite Solids

When the focus is on how a solid structure responds to an applied force, the resulting vibrations can be analysed to predict the radiated components of structure-borne sound into the surrounding environment. The different stages from excitation to radiation are illustrated in Figure 2.1 [7].

Waves propagating through solid structures behave differently from waves propagating through air. When sound pressure propagates through a concrete element, such as a slab or a pillar, the resulting motion is not limited to one-dimensional propagation. Instead, transverse forces and deformations occur in both the x and y directions [8]. These deformations give rise to motion patterns that resemble sinusoidal waves propagating through the structure [7].

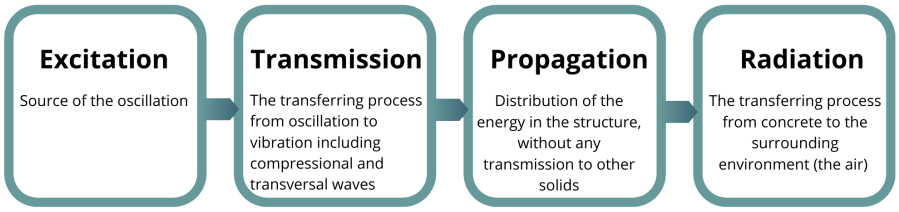

Figure 2.1: Shematic illustration of wave propagation in solids

2.3.1 The critical frequency in plates

The critical frequency f_c for a plate can be estimated using Equation 2.4, [9, pp. 240–244].

$$f_c = \frac{c_0^2}{2\pi h}\sqrt{\frac{12\rho(1-\nu^2)}{E}} \tag{2.4}$$

Here,

- f_c: Critical frequency [Hz]
- c_0: Speed of sound in air (m/s)
- h: Plate thickness (m)
- ρ: Material density (kg/m^3)
- ν: Poisson's ratio (–)
- E: Young's modulus (Pa)

2.3.2 Radiation Loss and Geometrical Energy Decay for $f > f_c$ in plates

The radiation loss factor for bending waves in a plate, valid for frequencies above the critical frequency ($f > f_c$), is given by the following formula 2.5 [7, p. 497]:

$$\eta_{\text{rad}} \approx \frac{\rho_0}{m''} \cdot \frac{1}{\sqrt{k_0^2 - k_B^2}} \tag{2.5}$$

Here, ρ_0 is the density of the surrounding medium (e.g., air), m'' is the mass per unit area of the plate, k_B is the bending wave number, and k_0 is the acoustic wave number in air.

For $f > f_c$, the surrounding fluids, such as air, result in a small η_{rad}. Consequently, radiation attenuation is primarily influenced by geometrical decay for a certain distance from the source expressed as r, and is described below [7, p. 497]:

$$|v(r)|^2 \propto \frac{1}{r} \tag{2.6}$$

2.4 From Vibration to Radiation for a Surface

When a structure is set into vibration, the resulting airborne sound radiation carries significant information about the normal velocity distribution of the vibrating surface. From an engineering perspective, the radiated sound power can be derived by analysing the transfer of energy from one-dimensional plane waves propagating through a solid and coupling into the surrounding air. The radiated sound power can be expressed as a formula 2.7 [9, p. 238].

$$W_{\text{rad}} = \rho_0 c_0 S \left\langle v^2 \right\rangle \sigma \tag{2.7}$$

Here,

- S is the total surface area
- $\rho_0 c_0$ is the acoustic impedance of air
- $\langle v^2 \rangle$ is the surface-averaged mean-square normal velocity
- σ is called the radiation ratio or radiation efficiency

2.5 Wave Propagation in a Concrete MDOF System

The different ways of describing vibrations in multi-degree-of-freedom systems (MDOF) can involve both wave propagation and mode shapes in the system. In this context, the modes represent constructive interference of the waves. There are several ways of studying how waves are transported through a structure [9].

Wave propagation in MDOF systems largely depends on the amplitude of the bending waves travelling through the structure. These waves cause two-dimensional deformations, where the displacement occurs in the direction normal to the surface of a structure, such as a beam or a plate. However, bending waves in beams versus plates will tend to differ in their propagation patterns. If cross-sectional deformations are neglected, the effect on the element can be described using different theories depending on the geometry of the structure [8].

Vibrational Analysis of Beams Using Euler–Bernoulli Theory

Shear deformations and rotational inertia for a cross-section is negligible to simplify the pattern of a thin beam. Transverse and longitudinal loads will act on the centre line of the beam [9].

The equation of motion is based on deformation in one dimension and can be seen in Equation 2.8 for a beam according to the Euler-Bernoulli theory [8, p. 27]:

$$\frac{\partial^2}{\partial x^2}\left(B(x)\frac{\partial^2 \eta}{\partial x^2}\right) + m\frac{\partial^2 \eta}{\partial t^2} = 0 \tag{2.8}$$

Vibrational Analysis of plates Using Kirchhoff Theory

In plates, there is a two-dimensional deformation, and the theory of the motion of particles inside the solid is based on Euler´s assumption of an unchanged cross-section, see Equation 2.9, [8, p. 29].

$$B_x\frac{\partial^4 \eta}{\partial x^4} + 2B_{xz}\frac{\partial^2}{\partial x^2}\frac{\partial^2 \eta}{\partial z^2} + B_z\frac{\partial^4 \eta}{\partial z^4} + m\frac{\partial^2 \eta}{\partial t^2} = 0 \tag{2.9}$$

2.6 Longitudinal and Transversal Waves in Concrete Structures

The longitudinal waves create a volume change, and their velocity plays a crucial role in the resulting deformations within the structure. In finite structures, stress can be retained even when no continuous external force is applied. Impact sources, such as an impact hammer excitation, therefore contribute to longitudinal stress

fields in the material [7].

The velocity of longitudinal waves in a plate is given by Equation 2.10, which shows that the wave speed depends on the material's Young's modulus E, density ρ, and Poisson's ratio ν [9, p. 289].

$$c'_L = \sqrt{\frac{E}{\rho(1-\nu^2)}} \tag{2.10}$$

Here,

- c'_L: Longitudinal wave velocity in the plate (m/s)
- E: Young's modulus (Pa), a measure of the stiffness of the material
- ρ: Density of the material (kg/m^3)
- ν: Poisson's ratio (dimensionless), describes the ratio of lateral to axial strain

2.7 Bending Waves and Their Importance

In terms of radiation from different structures, bending waves play the most important role in the deformations caused by propagating waves within a structure. The main reason for this is that bending waves create deformations in two-dimensional directions, where the primary deformations and tensions occur in the normal direction to a surface exposed, and the boundary conditions are more complex than for the longitudinal waves [7, p. 49].

An essential feature of bending waves is their dispersive nature, which causes wave velocity to increase with frequency. This relationship is expressed by the phase velocity c_B, in Equation 2.11 [7, p. 55].

$$c_B = \sqrt[4]{\frac{B}{m'}\,\omega^2} \tag{2.11}$$

Here, c_B is the phase velocity of the bending wave, m' is the mass per unit length, and k is the wave number.

An important additional parameter is the wavelength of the bending wave λ_B, which is derived from the bending wave number k. According to the theory of bending wave propagation in plates, the wave number is given by Equation 2.12 [9, p. 241]. The bending wavenumber k_B can be expressed as:

$$k_B = \left(\frac{\mu\omega^2}{D}\right)^{1/4} \tag{2.12}$$

Here, $\mu = \rho h$ is the mass per unit area and D is the bending stiffness per unit width, defined in formula 2.13 [9, p. 241]:

$$D = \frac{Eh^3}{12(1-\nu^2)} \tag{2.13}$$

Here,

- E is the Young's modulus [Pa]
- h is the thickness of the plate [m]
- ν is the Poisson's ratio (-)

And from the wavenumber, the bending wavelength λ_B is given by formula 2.14 [9, p. 241]:

$$\lambda_B = \frac{2\pi}{k_B} \tag{2.14}$$

2.7.1 Geometrical Attenuation, Material Loss Factors and Their Impact on Energy Decay

An analytical expression for the decay of vibration level in free bending waves, accounting for both geometrical spreading and material damping, is presented by Cheng [5, pp. 12–13]. The expression describes the level $L_B(r)$ at distance $r \geq 1\,\mathrm{m}$ in equation 2.15 as:

$$L_B(r) \approx -N \log_{10}(r) - \frac{4.34\pi\eta}{\lambda_B} r \tag{2.15}$$

Here:

- N is the geometric spreading factor, with $N = 10$ for cylindrical (2D) propagation and $N = 20$ for spherical (3D) propagation,
- η is the internal material loss factor,
- λ_B is the wavelength of the bending wave,
- r is the distance from the excitation point (m).

To generalise this relationship further, an analytical expression can be formulated using the group velocity c_{gB} and the angular frequency ω, as shown in Equation 2.16 [5, p. 13].

$$L_B(r) = -N \log_{10}(r) - \frac{N}{\ln(10)} \cdot \frac{\omega \eta_{\mathrm{int}} r}{c_{gB}} \tag{2.16}$$

In this formulation, c_{gB} denotes the velocity at which energy travels through the structure (m/s), and ω is the angular frequency in radians per second.

2.8 Experimental Determination of Loss Factors and Reverberation Time in SDOF systems and for airborne sound

The reverberation time in single degree of freedom (SDOF) systems can be linked to the internal loss factor of energy dissipation within the system, see Equation

2.17. To validate the reverberation time and other variables, such as the loss factor of a structure in experimental settings, the following formulas can be applied when the system is excited by a constant force. Although this theory is specifically derived for single-degree-of-freedom (SDOF) systems, multi-degree-of-freedom (MDOF) systems will require additional considerations [8, p. 64].

$$T = \frac{2.2}{\eta f} \tag{2.17}$$

And by solving for η, the loss factor of the system is:

$$\eta = \frac{2.2}{Tf} \tag{2.18}$$

2.9 Modal-Analysis

Modal analysis is used to create a model of a building's dynamic behaviour. By using the building's material properties and dimensions, one can predict which modes the building will experience the largest displacement from [10].

2.9.1 Modal Superposition and Modal Synthesis

The modal approach provides various methods to analyse the vibrational patterns of a structure. When the goal is to calculate the displacement or velocity at a specific position within the structure, one can apply the derivation for modal summation, provided the excited eigenfrequencies are known. This method can be utilised in the frequency response function $H_n(x, \omega)$ of an impulse response, as described in 2.19. The formula is derived from *Propagation and Radiation of Structure-Borne Sound* [8] and [11, pp. 326–332]. Using modal superposition, the frequency response function between an excitation point x_0 and a receiver point x_r can be approximated by:

$$H(x_r, \omega) = \sum_{n=1}^{N_m} \frac{F_e \cdot \Phi_n(x_r)\Phi_n(x_0)}{\omega_n^2 - \omega^2} \tag{2.19}$$

Here,

- F_e is the excitation force
- $\Phi_n(x_r)$ and $\Phi_n(x_0)$ are the modal acceleration values obtained from Comsol at the receiver and excitation points,
- $\omega_n = 2\pi f_n$ are the eigenfrequencies of the structure for a specific mode n,
- $\omega = 2\pi f$ is the angular frequency of the input signal.

Equation 2.19 is the core of the analysis that will be done on the data generated from the Comsol models. Figure 2.2 illustrates a typical example of the impulse response curves generated from Equation 2.19.

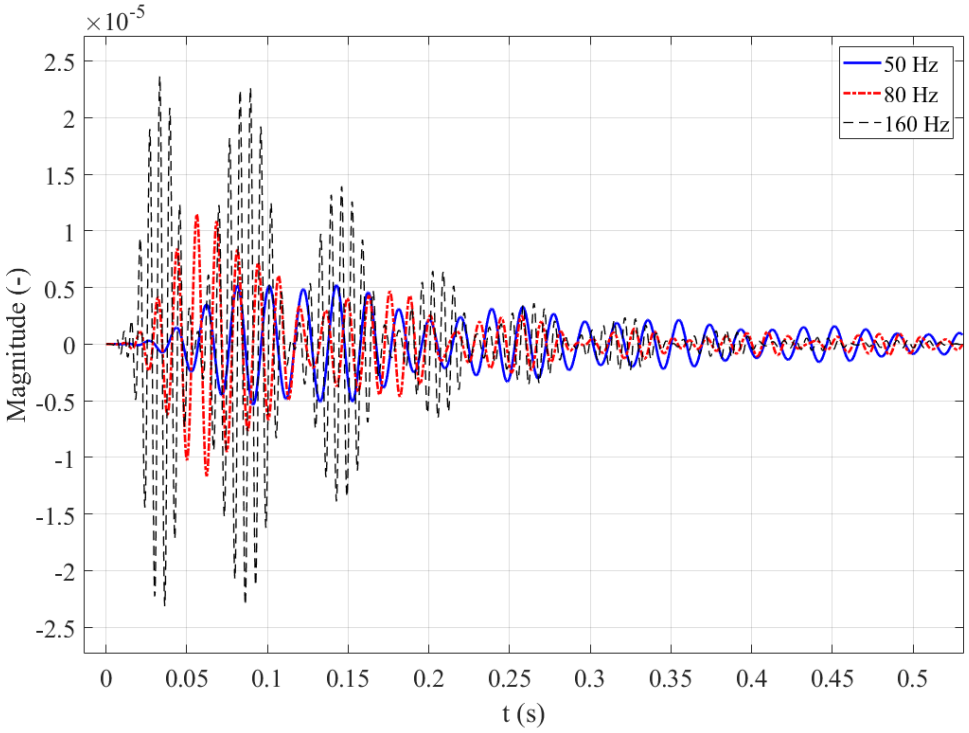

Figure 2.2: An impulse response, generated using Equation 2.19, was created based on mode shapes from a free-free, 10 m concrete beam modelled in Comsol. The mode shapes are complex and originate from a single point on the beam, x_r, and normalized with the mode response from the excitation point, x_0. The response has been filtered into third-octave bands.

The results from Equation 2.19 give the displacement from mode shapes. This can also be interpreted as the creation of a synthetic frequency response function for a structure. For low frequencies, a few modes are often adequate for an accurate representation of the vibrational response. Low eigenfrequencies are usually well established through the finite element method analysis [7].

2.9.2 Calculations in Comsol Multiphysics

The Finite Element Method and Meshing Size

The simulations in this master's thesis are carried out using the finite element method, a well-established calculation model commonly used in modern physics-based simulation software. It discretises the governing partial differential equations (PDEs) of various physical phenomena—such as structural displacements, heat flux, and vibrations—into a large but finite system. In this context, vibrations refer to the mechanical oscillations of the structure [12].

FEM is applied by partitioning the geometry of a structure into a mesh of finite elements. Each element interacts with its neighbours through shared nodes, and together they approximate the behaviour of the entire structure. The mesh den-

sity—and thus the numerical accuracy—is determined either by the user or by automatic refinement settings specified for a particular calculation [12].

Eigenfrequency Analysis

Comsol Multiphysics is a software that allows computer simulations of coupled physical phenomena involving multiple interacting processes [13]. In this master's thesis, the main part used is the structural mechanics module's eigenfrequency analysis. This analysis can be used to retrieve mode shapes, $\Phi(w)$, that can be used for analysis based on modal superposition. The eigenvalues can be undamped see Equation 2.20, damped see Equation 2.21, and complex see Equation 2.22. Here, m is the mass, k is the stiffness coefficient, ζ is the damping ratio, and η is the loss factor [14].

$$\omega_0 = \sqrt{\frac{k}{m}} \tag{2.20}$$

$$\omega_d = \omega_0\sqrt{1-\zeta^2} \tag{2.21}$$

$$\omega_c = \omega_0\sqrt{1+i\eta} \tag{2.22}$$

For each eigenfrequency there is a mode shape, ϕ, which is the shape of the deformations that appears when an eigenfrequency is excited. If the eigenfrequency is complex, the associated mode shape will also be complex-valued. A complex eigenfrequency consists of angular frequency, ω, and the imaginary part that contains information about the damping. The respective mode shape has complex-valued displacements, which include phase information. This is because damping causes phase shifts at different parts of the structure being analysed [14].

2.9.3 Loss Factors

When the sound is studied in structures, the damping is not proportional to the velocity but proportional to the displacement[8]. The damping can be written as a complex stiffness such as shown below in Equation 2.23 [8, p. 7]:

$$s = s' + js'' \quad \text{or} \quad s = s'(1+j\eta) \tag{2.23}$$

Here, η is the loss factor, defined as the ratio of the energy lost per cycle to the total reversible (stored) energy, as shown in Equation 2.24.

$$\eta = \frac{E_{\text{loss}}}{2\pi E_{\text{reversible}}} \tag{2.24}$$

2.10 Data Processing

This section describes the tools and processes used for the data processing.

2.10.1 The Fast Fourier Transform and the Inverse Fourier Transform and Their Consequences

The Fourier Transform is used to determine the spectral components of time signals. These components are obtained by decomposing the time-domain signal into sinusoids and cosinusoids, each defined by its magnitude and phase. The Fast Fourier Transform FFT is an optimized algorithm for computing the Discrete Fourier Transform DFT. The FFT is more efficient than a direct DFT because it has lower computational complexity [9, pp. 164–169]. In this thesis, the FFT is applied via the built-in `fft` function in Matlab.

The Inverse Fast Fourier Transform IFFT is used to reconstruct a time-domain signal from its frequency-domain representation. In Equation 2.25, the signal $x(t)$ is expressed as a Fourier integral, while Equation 2.26 shows the corresponding frequency-domain form $X(f)$ [9, pp. 147–151]. Matlab also provides the matching `ifft` function for this inverse step.

$$x(t) = \int_{-\infty}^{\infty} X(f) e^{i2\pi ft}\, df = \mathcal{F}^{-1}\{X(f)\} \tag{2.25}$$

$$X(f) = \int_{-\infty}^{\infty} x(t) e^{-i2\pi ft}\, dt = \mathcal{F}\{x(t)\} \tag{2.26}$$

As mentioned in Section 2.9, a Frequency Response Function FRF is constructed from mode shapes using Equation 2.19. With the use of the IFFT, and given a known frequency resolution, an impulse response can be created in the time domain.

Since the mode shapes contain both magnitude and phase, and $\Phi(\omega)$ is non-linear to ω, i.e., the system is dispersive. The group delay becomes frequency-dependent, and a phase delay between frequency components will appear in the time domain [9, p. 151].

2.10.2 The Reshaping of Signals Through Deconvolution

Starting with convolution, it takes two separate signals in either the frequency domain or in the time domain, and produces a third signal. If $x(t)$ is a time-dependent signal and $h(t)$ is a time-dependent system impulse response, the convolution of the two signals will create an output signal $y(t)$ [9, pp. 152–153]. This is commonly written in the form of Equation 2.27. An important requirement is that the system is linear and time-invariant [15].

$$y(t) = x(t) * h(t) \tag{2.27}$$

Convolution is less complicated to perform in the frequency domain, meaning that before doing the convolution, using the FFT on it is advised, turning Equation 2.27 into 2.28.

$$\underline{Y}(f) = \mathcal{F}\{x(t)\} \cdot \mathcal{F}\{h(t)\} = \underline{X}(f) \cdot \underline{H}(f) \tag{2.28}$$

Here $\underline{Y}(f)$, $\underline{X}(f)$ and $\underline{H}(f)$ are the complex-valued, Fourier transforms of $y(t)$, $x(t)$ and $h(t)$.

Deconvolution is the inverse of that. Using Equation 2.28 it is now possible to define $\underline{H}(f)$ as the following equation:

$$\underline{H}(f) = \frac{\underline{Y}(f)}{\underline{X}(f)} \tag{2.29}$$

Now using Equation 2.26 gives the system impulse response shown in equation 2.30:

$$\mathcal{F}^{-1}\{\underline{H}(f)\} = h(t) \tag{2.30}$$

This is useful if a measurement on a system was made that produced an input signal $x(t)$ and an output signal $y(t)$, and the system impulse response, $h(t)$, is of interest [15].

2.10.3 Tools of the Time-delay Interpretation, Backwards-integration and Cross-correlation

Cross-Correlation

The cross-correlation of the two signals for an input and an output LTI system and it allows for defining the time lag between two events. See Equation 2.31 and 2.32, which are equivalent to each other, but show that the lag, l, can be both at x and y. The term n is the sample number for signals x and y.

$$r_{xy}(l) = \sum_{n=-\infty}^{\infty} x(n)\, y(n-l), \quad l = 0, \pm 1, \pm 2, \ldots \tag{2.31}$$

$$r_{xy}(l) = \sum_{n=-\infty}^{\infty} x(n-l)\, y(n), \quad l = 0, \pm 1, \pm 2, \ldots \tag{2.32}$$

The subscript for r, shows in what order the delay occurs in, for r_{xy} it goes from x to y and vice versa for r_{yx}. This yields Equation 2.33.

$$r_{xy}(l) = r_{yx}(-l) \tag{2.33}$$

This means that $r_{yx}(l)$ is just the folded version of $r_{xy(l)}$ with $l = 0$ as the folding point and that both expressions give the same information under the right circumstances [16, pp. 120–125].

Centre Time of Gravity

The centre of gravity time, expressed as t_c, of a recorded signal $y(t)$, is defined as the time it takes for the energy from an impulse to reach a measuring point that corresponds to the centre of gravity of that energy. This concept is useful for

identifying where the signal reaches its maximum value. In the continuous case, a signal can be described using Equation 2.34:

$$t_c = \frac{\int_{-\infty}^{\infty} t\, y(t)\, dt}{\int_{-\infty}^{\infty} y(t)\, dt} \tag{2.34}$$

Here, the condition $y(t) \geq 0$, $\forall t \in (-\infty, \infty)$, must be fulfilled.

When recording signals in practice, the signals are discrete and sampled over a specific interval in the time domain. The gravity centre of the recorded discrete signal is then calculated according to Equation 2.35 [17].

$$t_c = T_s \cdot \frac{\sum_{k=1}^{N} k\, y[kT_s]}{\sum_{k=1}^{N} y[kT_s]} \tag{2.35}$$

Here, T_s represents the sampling period of the signal.

2.10.4 Filtering by Third-Octave Bands

The filtering of signals into third-octave bands can be done in Matlab using the `octaveFilterBank`. It decomposes the signal into octave or fractional-octave bands, where each octave band spans a frequency range in which the upper frequency is twice the lower frequency [18].

2.10.5 Distance Approximation

When measuring distances in three-dimensional spaces, various methods can be utilised. To effectively approximate the distance within a building, it is essential to find the shortest path possible, ensuring that the measurements align with the Praxis energy transportation assumption in physics. One method commonly used for predicting what are known as the Euclidean distance method, which is applicable in two-dimensional spaces [19].

The Euclidean distance between two measurement positions in two-dimensional space is defined in [19] and described in Equation 2.36.

$$r = \sqrt{(x_r - x_0)^2 + (y_r - y_0)^2 + (z_r - z_0)^2} \tag{2.36}$$

Here, x_r is the measurement point and x_0 is the excitation point.

3
Method

This study combines in-situ measurements and numerical simulations to investigate how structure-borne vibrations propagate in concrete buildings. In this context, vibrations refer to the mechanical oscillations of structural elements. Comsol Multiphysics was used to simulate a simplified building structure model, allowing a controlled analysis of the vibrational behaviour across multiple floors and distances throughout a concrete building. The simulations aimed to verify whether key trends observed in real measurements, such as level decay and effective group velocity, could also be reproduced in a known, idealised model.

The in-situ measurements were carried out at the real office building at Hovfaret 17 in Oslo, where a shaker was used to excite the concrete structure. These measurements provided data on vibrational level decay L_a over distance and energy distribution across the structure, which served as reference points for the validation of the numerical results.

The modal approach, implemented in Comsol and post-processed in Matlab, was used to generate impulse responses based on the eigenfrequencies of the real office building in Oslo. By applying modal superposition and inverse Fourier transforms, time delays between different points in the structure were estimated and compared to the in-situ measurement data.

3.1 Model Description for the In-Situ Office Building

The model represents the structural skeleton of the building, with calculations limited to the substructure where the office is located and where the measurement was conducted, as shown in Figure 3.6. The dimensions for the structure were taken from existing construction sketches made by Ingenieur Bonce CO. (1961-11-13) [20]. Parameters not provided were assumed based on current ISO standards and typical building practices, which can be found in Table 3.1. The table also presents the critical frequency of the slab f_c.

Property	Symbol	Value	Source/Comment
Density	ρ	2300 kg/m^3	Engineering practice (2300–2500 kg/m^3)
Young's modulus	E	30 GPa	SS-EN 1992-1-1:2005, Table 3.1 (C20/25)
Poisson's ratio	ν	0.20	Engineering practice [7]
Thermal expansion	α	10×10^{-6} 1/K	SS-EN 1992-1-1:2005, Clause 3.1.3(5) [21]
Thermal conductivity	k	1.8 W/m·K	Engineering practice
Specific heat capacity	c_p	880 J/kg·K	Engineering practice
Loss factor (complex)	η	0.05	Estimated value used for damping in harmonic analysis
Critical frequency	f_c	34 Hz	Calculated using Equation 2.4

Table 3.1: Material properties used in the simulated model together with the critical frequency for the slabs in the in-situ office building.

The dimensions of the various office elements are listed below in Table 3.2. This was used as a reference for the Comsol simulations.

Structural Element	Dimension(s)	Comment
Floor (slab)	0.15 m (thickness)	Uniform across all floors
Beams	0.35 m × 0.35 m (width × height)	Uniform cross-section
Pillar	0.35 m × 0.35 m (width × depth)	Square cross-Section
Load-bearing wall	0.15 m (thickness)	Uniform thickness

Table 3.2: Geometrical dimensions used in the Comsol model for different elements.

The model was developed using Comsol. An overview of the entire building complex, including the specific case study structure, is illustrated in Figures 3.1 and 3.2.

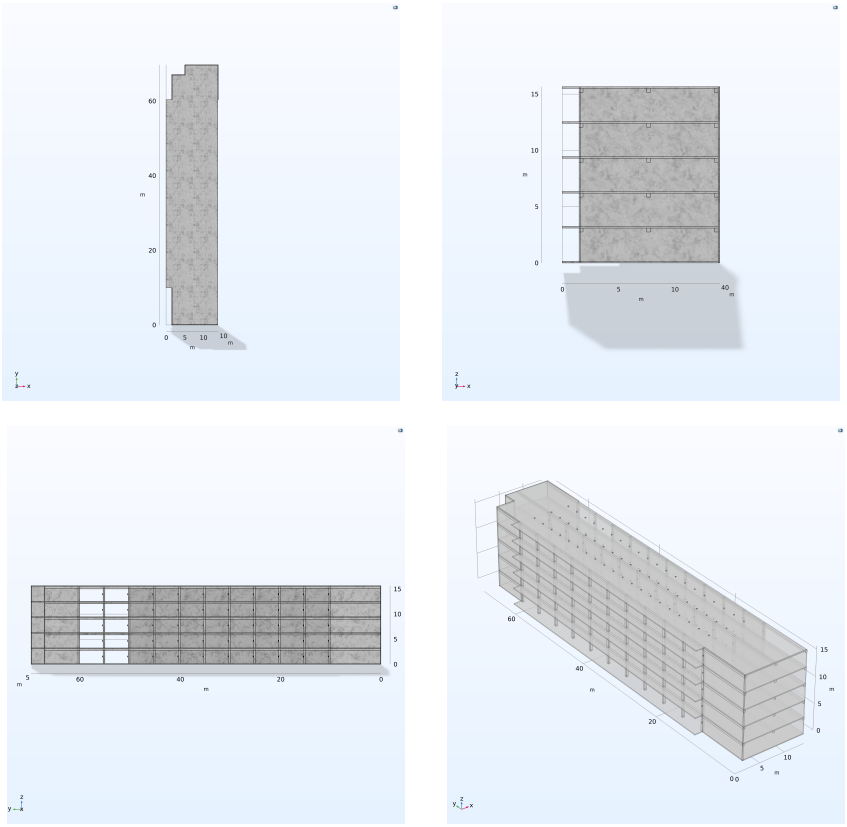

Figure 3.1: 2D top, side, front, and 3D visualizations of the substructure analysed in this study.

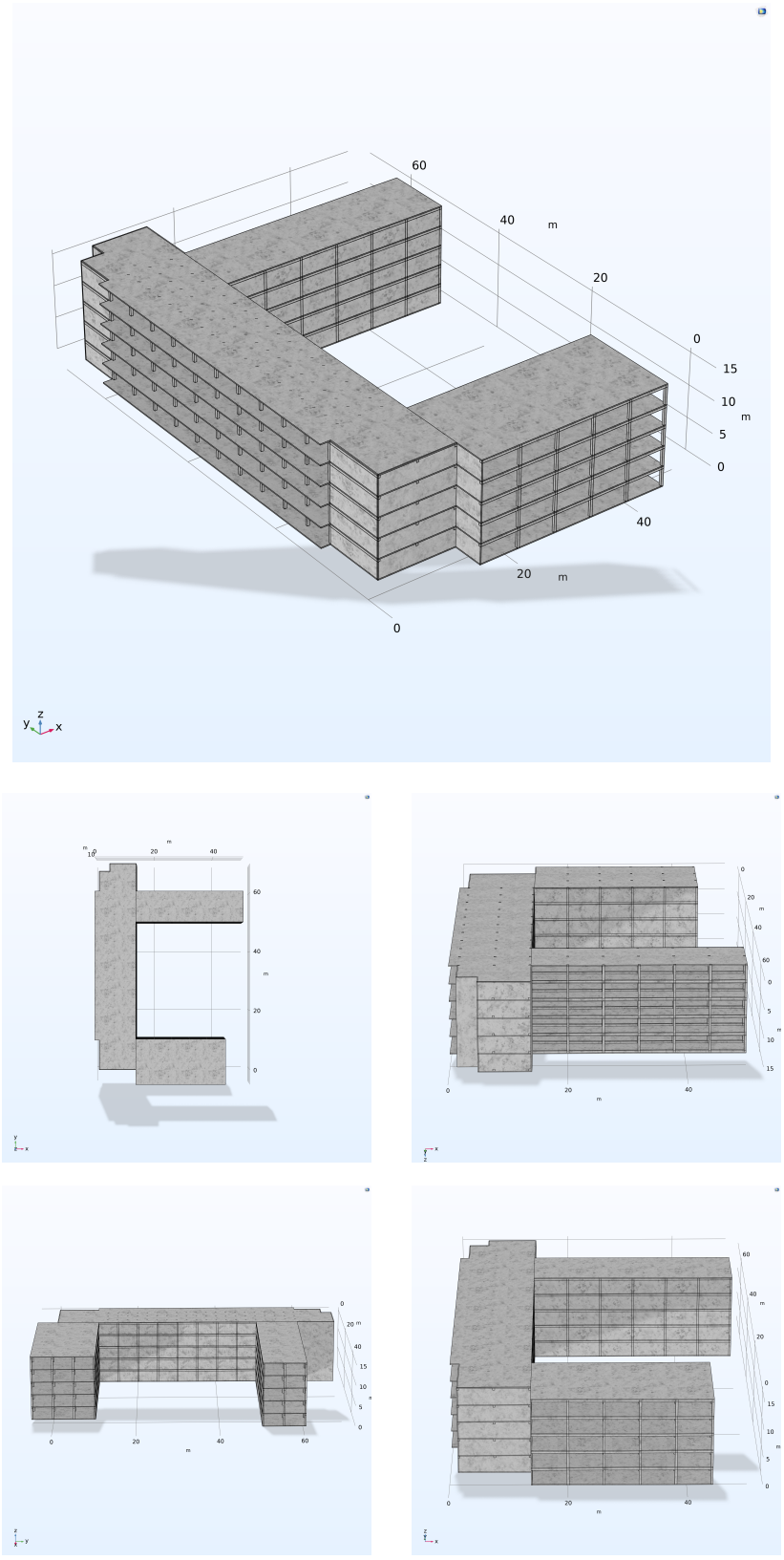

Figure 3.2: 2D and 3D visualizations of the full building structure modelled in Comsol.

3.2 Numerical simulations in Comsol Multiphysics

Simulations of the system were performed in Comsol using a modal approach, as previously described. Based on the background of this study, eigenfrequencies were of particular interest around 63 Hz, as this frequency belongs to a key third-octave band and is specifically highlighted by Brekke and Strand.

The number of eigenfrequencies reached up to 1200; the spread was even, and the lowest and highest frequencies were 2 Hz and 134 Hz, respectively. Due to computational time, a search with a larger number was not attempted. To obtain a correct impulse response from Equation 2.19, all eigenfrequencies needed to be retrieved in a single search. Discretising the search by third-octave bands would have resulted in gaps in the eigenfrequency vector, resulting in an incorrect impulse response.

The purpose of simulating the case study in Comsol was to provide a representative scenario in which the building system could be analysed on a larger scale. This enabled a more comprehensive study of the vibration field, including additional measurement points and greater distances. The aim was to investigate how effectively Comsol can be used to analyse vibrational behaviour in larger structures and to compare these results with in-situ measurements as well as analytical solutions.

The model itself was built in Comsol Multiphysics version 6.2 and was simplified both in its geometry and in the connections between elements. Only the portion of the building where measurements were conducted was considered. The model was fixed to the ground in all three translational directions. It represented the structural skeleton: beams, plates, walls, and pillars were modelled as solid concrete elements. A detailed specification of the model is provided in Table 3.1. The parameters followed Swedish standards according to Eurocode and are specified in SS-EN 1992-1-1:2005 [21], while some values were chosen according to praxis. The rest of the building complex is connected via lead couplings, allowing limited two-dimensional motion and free rotation; however, this connection was neglected in the simulation. The ground was also omitted due to computational time constraints. Internal energy losses were represented by a complex loss factor set to 0.05 [8].

Structural Element	Dimension(s)	Comment
Floor (slab)	0.15 m (thickness)	Uniform across all floors
Beams	0.35 m × 0.35 m (width × height)	Uniform cross-Section
Pillar	0.35 m × 0.35 m (width × depth)	Square cross-Section
Load-bearing wall	0.15 m (thickness)	Uniform thickness

Table 3.3: Geometrical dimensions used in the Comsol model for different elements.

The Solid Mechanics interface in Comsol was used to simulate the structural dynamics of the concrete structure, allowing the identification of eigenfrequencies and mode shapes. The structure was modelled as a homogeneous structure with evenly distributed stiffness and mass. The boundary conditions for the model are given below.

- **Fixed constraints** were applied on all of the surfaces and corners connected to the ground.
- **Free boundaries**: The rest of the building was simulated as free boundaries, meaning that no external load or displacements were applied to these parts.

3.2.1 Model Visualization

An overview of the Comsol model can be seen in Figure 3.2, showing the complete building structure with connecting substructures. There is an additional existing garage beneath ground level, as well as an additional sub-building connecting all of the buildings. However, this sub-building was not simulated or included in the calculation of the modal behaviour of the structure.

The substructure analysed in this study is the area where the office of Brekke & Strand is located, and it is illustrated in Figure 3.1. This part of the structure was selected because it corresponds to the area where the in-situ measurements were performed. The first floor is modelled with the same construction as the floors above, which follow the actual building's dimensions. However, the actual first floor has a different structure and boundary conditions than those used in the model. It corresponds to the basement of the building, to be able to still consider the basement in the calculations.

3.2.2 Measurement Point Distribution

The measuring points were distributed to capture the vibrational behaviour of most areas of the floors as well as the pillars. Refer to Table 3.4 for the specified distances of the measuring points, and see Figure 3.2 to visualise their distribution throughout the building on each floor. The measuring point on each pillar was positioned at the midpoint of its length. In total, there were 300 measurement points for the slabs and 165 for the pillars, making a grand total of 465 measuring points. The placement of the different measuring points does not correspond exactly to the specified locations, except for the excitation point, which is positioned at the same location as in the in-situ measurements. The excitation point is located on the third floor of the measured sub-structure illustrated in Figure 3.1.

Measurement Area and Point Distribution	**c/c Distance**
Floor (slab): 60 points per floor, floor (1–5)	3.5 m in x-direction, 2.5 m in y-direction
Pillar: 33 points per floor, floor (1–5)	6 m in x-direction, 5 m in y-direction

Table 3.4: Distribution of measurement points on floor slabs and pillar for floors 1 to 5, including center-to-center (c/c) distances in different directions.

3.2.3 Meshing

The size of the elements when modelling the meshing for different frequencies depends on the wavelength for bending waves. The meshing size is set to different values as a minimum element size condition due to the dispersive behaviour of bending

wave propagation in concrete structures, leading to different wavelengths for different frequencies [7]. A minimum element size corresponding to five elements per wavelength was preferred for the meshing of the structure [22]. However, applying this criterion resulted in excessive computational demands for the large structural model, and a coarser preset 'Fine' mesh size was used for the model instead. The preferred maximum element size for each frequency can be seen below in Table 3.5.

Mesh Size Parameter	Value (m)
Minimum element size	0.55
Maximum element size	5.58

Table 3.5: Mesh size range used in the simulations (Comsol 'Fine' preset).

3.2.4 Study Type

The solver in the eigenfrequency search was set to ARPACK to enhance a quicker simulation process. The default settings for tolerence in Comsol were used, which was set at 1×10^{-6} to ensure a high numerical accuracy for the computed eigenfrequencies and mode shapes.

3.3 In-situ measurements

In-situ measurements were conducted for an office building located at Hovfaret 17, 0275 in Oslo. This building is a mixed-use facility that includes a grocery shop, a garage, and various offices. The measurements took place on the third, fourth, and fifth floors. Although the measurement procedure did not follow a specific standard, calibration was performed for each piece of equipment used. The measurement took place on a day when all the premises were closed.

3.3.1 Measurement Objective

The objective of the measurement was to characterise the vibrational behaviour of the building structure by measuring acceleration at various positions throughout the building. The aim was to capture wave propagation using a three-axis accelerometer and a shaker as the excitation force, which would set the system into motion. The primary focus was to observe the vibrational behaviour over distance by controlling the force acting on the system, as well as through the distributed measurement points.

3.3.2 Procedure for on-site measurements

The method chosen to measure acceleration involved using a shaker with a sinusoidal sweep to achieve a high signal-to-noise ratio. This approach ensured that we generated a sufficiently strong signal throughout the entire structure when it was excited. The impulse was measured using two three-axis accelerometers. One accelerometer was positioned to capture the input acceleration, while the second was

moved around floors 3 to 5, on both the pillars and the slabs. This setup aimed to measure the acceleration in the z-direction, perpendicular to the floors and pillars, in order to capture the deformations caused by the bending waves propagating through the structure. The measurement procedure for the in-situ measurement is described below in arbitrary order.

1. The measurement set-up was mounted. See Figure 3.3 for photographs of the installation, Figure 3.5 for a schematic illustration, Figure 3.4 for the box diagram, and Table 3.6 for the measurement equipment specifications.

2. The shaker was placed on the third floor, and an accelerometer was mounted on top of the moving mass in the z-direction, perpendicular to the slab. This configuration was used to measure the input acceleration signal (reference), expressed in m/s^2.

3. The accelerometers were calibrated before the measurements. Both accelerometers were triaxial, measuring in the x-, y-, and z-directions. Calibration ensured accurate readings of acceleration signals in m/s^2.

4. The triaxial accelerometer was placed at varying distances from the shaker, oriented perpendicular to the surface of the slabs and pillars. Acceleration levels were recorded at each position for use in decay analysis and estimation of effective wave propagation.
   (a) Measurements started with the pillars.
   (b) The procedure continued on the third-floor slab, where the accelerometer was mounted on metal studs that were directly attached to the concrete structure.

5. Measurements on the fourth floor were performed.
   (a) The accelerometer was transferred through a window to the forth floor. Measurements began on the slab, where both metal studs and baseboards were available for mounting.
   (b) The pillars on the fourth floor were then measured.
   (c) Finally, the slab of the fifth floor was measured by placing the accelerometer on the ceiling base of the fourth floor.

6. Background acceleration measurements, expressed in m/s^2, were measured on the fourth and fifth floors using the accelerometers. These background measurements ensured that no unintended structural excitation or environmental vibrations affected the primary data collection.

Figure 3.3: Measurement setup and accelerometer placements. Top: overview of the equipment used. Middle left: accelerometer on the shaker, middle right: on pillar (P7). Bottom left: on the floor slab (M1). Bottom right: on the roof structure (M23).

3.3.3 Measurement Setup

The measurement setup consisted of a shaker that was placed on the third floor, which produced a sinusoidal wave around 63 Hz in constant periods. The data from the measurements was recorded using by using a Squadriga III with a sample frequency of 51.2 kHz.

Two accelerometers were used in the measurement campaign:

- One accelerometer mounted on the shaker, serving as a reference sensor to monitor the input signal.
- One movable accelerometer, which was repositioned between measurement points to record the structural response across different locations on the floor slabs and pillars.

Material

Table 3.6 has a list of the specified equipment used for the shaker measurement.

Item	Type of Equipment	Model	Purpose
1	Shear accelerometer	PCB Piezotronics	Measure acceleration (m/s^2) in x, y, and z direction
2	Sweep function generator	Hung Chang: 9205	Sinus-sweep generator
3	Power amplifier	APS: 145	Shaker amplifier
4	Vibration calibrator	MMF: VC21	Calibrated accelerometers
5	Squadriga	SQuadriga III	Data collector
6	Shaker	APS: 113	Excitation device
7	Skaker wieght (90 kg)	APS Reaction Mass	Added mass to shaker
8	Cables	BNC cables	Connecting equipment

Table 3.6: List of equipment used for the measurement.

The box-diagram for the equipment is shown in Figure 3.4. A simplified illustration of how the shaker measurement setup can be seen in Figure 3.5.

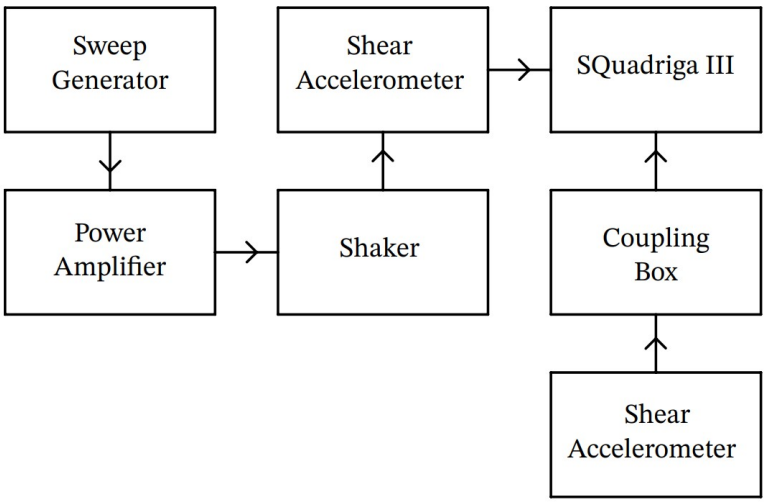

Figure 3.4: Box diagram for shaker measurement setup.

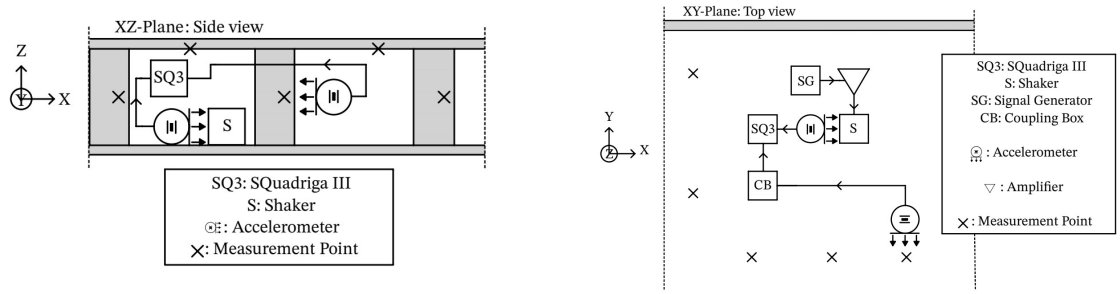

Figure 3.5: Illustrative side view (left) and top view (right) of the shaker measurement setup.

3.3.4 Measurement Points

The measuring points were strategically selected to ensure that the positions are distributed in all directions along the three axial dimensions, providing a representative result for the entire substructure. Resulting in 25 measurement positions for the slabs and 23 for the pillars, as illustrated in Figure 3.6. The sketch has been redrawn in Revit [23] and Bluebeam [24] from the fire sketch created by OPAK (2017) [25].

Measurement positions on floor 3 (slab and pillars)

Measurement positions on floor 4 (slab and pillars)

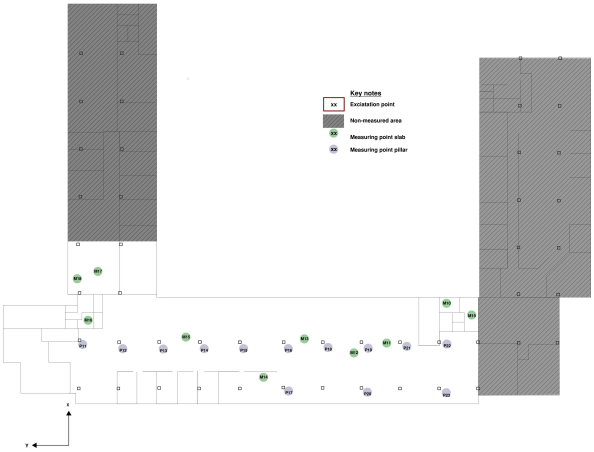

Measurement positions on floor 5 (slab and pillars)

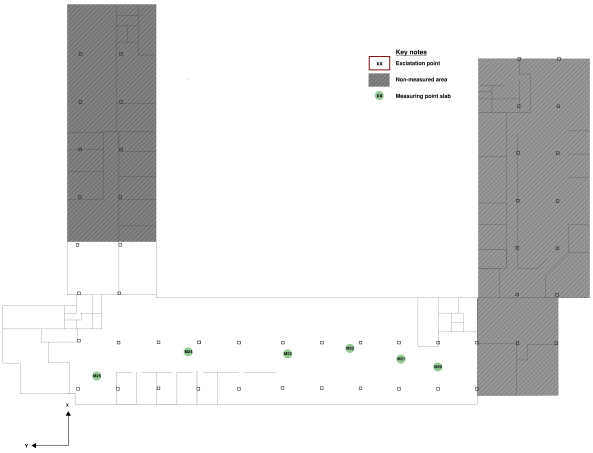

Figure 3.6: Measurement positions on slab and pillars for floors 3–5.

The Euclidean calculated distances (r) from the excitation point and the measurement points can be seen down below in Table 3.7.

Slab			Pillar		
Floor	**Meas. pt.**	**Dist. (m)**	**Floor**	**Meas. pt.**	**Dist. (m)**
3	exc	0			
3	M1	10	3	P1	9
3	M2	4	3	P2	4
3	M3	2	3	P3	4
3	M4	5	3	P4	8
3	M5	11	3	P5	12
			3	P6	12
			3	P7	8
			3	P8	4
			3	P9	4
4	M6	9	4	P10	9
4	M7	6	4	P11	37
4	M8	14	4	P12	32
4	M9	11	4	P13	27
4	M10	4	4	P14	22
4	M11	6	4	P15	18
4	M12	11	4	P16	13
4	M13	14	4	P17	13
4	M14	24			
4	M15	37			
5	M16	40	5	P18	9
5	M17	36	5	P19	5
5	M18	40	5	P20	6
5	M19	13	5	P21	6
5	M20	10	5	P22	9
5	M21	8	5	P23	10
5	M22	8			
5	M23	13			
5	M24	24			
5	M25	35			

Table 3.7: Calculated Euclidean distances from the excitation source to all measurement points on slabs and pillars for floors 3–5.

3.3.5 Potential Trouble-shooting

During the measurement, all other businesses were closed. However, there was a store on the first floor that had consistently operating low-frequency machines, such as freezers, which could affect the recordings. The measurement points were limited by cable length, allowing a maximum distance of 40 meters. Most points were placed closer to the source. The distance gap between 15 meters and 24 meters may

affect the evaluation of results in that range. However, a distance greater than 24 meters from the excitation point could not be achieved due to limitations in the signal-to-noise ratio (SNR).

3.4 Data Processing

The data processing was similar for both the measured data and the simulated Comsol data, except at the beginning. The Comsol data originated from the FEM analysis and the mode shapes generated in Comsol, while the measured data came from the accelerometers. Before obtaining impulse responses from both datasets, different steps were required, as explained in Section 3.4.1. The remaining post-processing is described in Section 3.4.2.

3.4.1 Impulse response calculations

This section describes the impulse response calculations.

Comsol Simulations

- The complex mode shapes in acceleration for the z-direction (normal to the surfaces) were exported from Comsol and analysed in Matlab using a modal approach.
- The complex eigenfrequencies and corresponding mode shapes were also exported, spanning the frequency range from 4–134 Hz. These were used to construct an FRF, as shown in Equation 2.19.
- Normalisation was performed with respect to the acceleration at the excitation point.
- The resulting FRF was used to compute the impulse response in the time domain using the IFFT.
- The impulse responses were split into third-octave bands using an octave filter bank in Matlab.

In-situ Measurements

- The distances for each measurement position were calculated using the Euclidean distance formula between the excitation point on floor 3 x_0, and each measurement point on both the slabs and the pillar. Equation 2.36 was used, and due to the three-dimensional movement in the z-direction, an additional term was included to account for this spatial component when calculating the distances across floors 3 to 5. The distances for each measurement point are listed in Table 3.7.
- The spectrograms of each impulse response were calculated to identify which frequencies were most strongly excited by the shaker. See Appendix A.2, A.3, and A.4.
- The measurement data were loaded into Matlab.

- The impulse responses were created through deconvolution using the following expression:
$$IFFT\left(\frac{FFT(\text{Point}_{\text{Measurement}})}{FFT(\text{Point}_{\text{Excitation}})}\right).$$
- The resulting impulse responses were filtered into third-octave bands, and the resulting system response curves were backward-integrated.

3.4.2 Common Post-Processing

The data processing for the in-situ measurements and Comsol simulations is presented below. This chapter describes the overall data processing steps for both the Comsol simulations and the in-situ measurements. The steps were carried out in the following order:

- All post-processing was performed in Matlab.
- Slabs and pillars were analysed separately due to their differing structural behaviours: slabs exhibit plate-like characteristics, while pillars behave more like beams (see Chapter 2.5).
- All results were initially normalised to the measured acceleration on top of the shaker at the excitation point, defined as the reference position x_0. However, for the analysis of the vibrational level L_a as a function of distance, the data were subsequently re-normalised to the measurement point located closest to the source (typically M3, at approximately 2 m in the in-situ measurements, and point 28 in Comsol, located approximately 2.5 m from the excitation source). This adjustment was made to enable more consistent comparisons between measurements and simulations, as the shaker-mounted reference point showed greater variability. For all other analyses, the original reference at $x = x_0$ was maintained.
- Backward integration was applied to the impulse response to estimate the reverberation time for each third-octave band and for all receiver positions, specified in detail below in Section 3.4.3.
- Additional parameters derived from the impulse response include: time delay, magnitude decay over distance, and effective group velocity.
- The T_{60} estimation between -1 dB from max L_a and -61 dB from max L_a was performed using the T_{60} method.
- The mean value of the structural reverberation time was calculated for all frequency bands.
- The equation for the centre of gravity time t_c for discrete signals was derived and implemented in Matlab.
- Five fitting cases were evaluated using the `fminsearch` function in Matlab to determine which model best describes the propagation of structure-borne waves in the slab system for the measured data:
  - **Case 1:** Geometrical spreading only
  - **Case 2:** Damping only
  - **Case 3:** Combined spreading and damping
  - **Case 4:** Cylindrical spreading with damping ($N = 10$)

  - **Case 5:** Spherical spreading with damping ($N = 20$)
- The time delay of the direct sound was determined by calculating the centre of gravity from the backward integration curves. This defines the time it takes for the direct sound to reach the reverberation field at each measurement point from the excitation source.
- The effective group velocity ($c_{g,\text{eff}}$) was estimated using both the time delay from processed data and the analytical solution using `fminsearch`.
- The results from the Comsol simulations were compared to both the in-situ measurement data and the analytical solution.

3.4.3 Backward Integration and Structural Reverberation Time

The impulse response data—examples of which are shown in Figures 3.7 and 3.8—were backward integrated, and the reverberation time was calculated from the resulting curves. This process forms the backbone of our analysis, from which most of the results are derived.

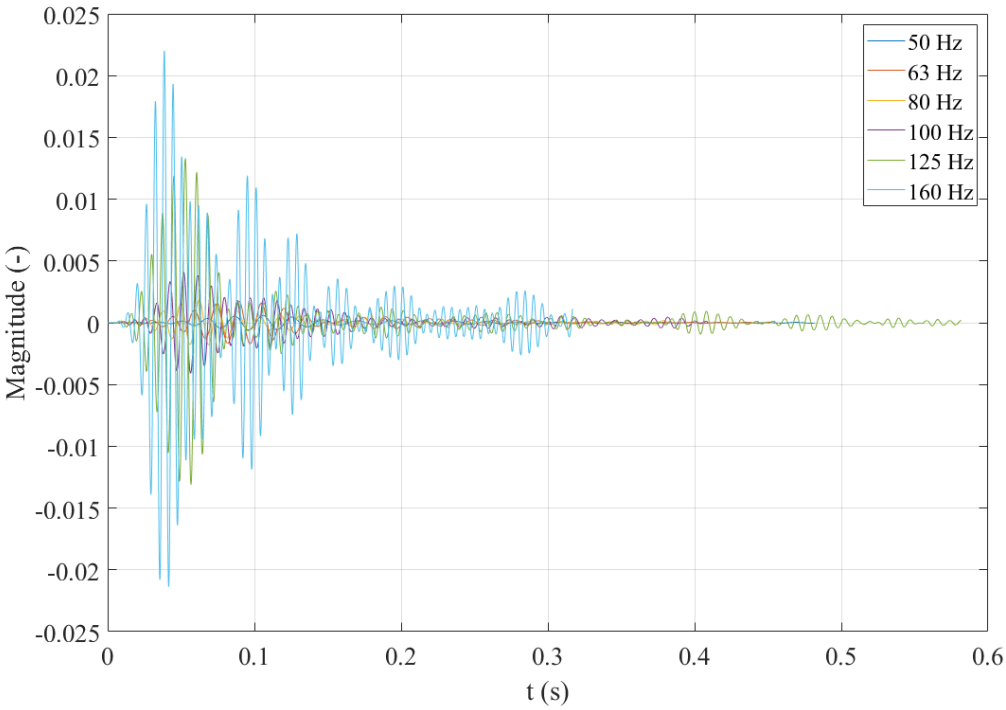

Figure 3.7: The impulse response at a single point from the measured data from the office building, filter into six third-octave bands.

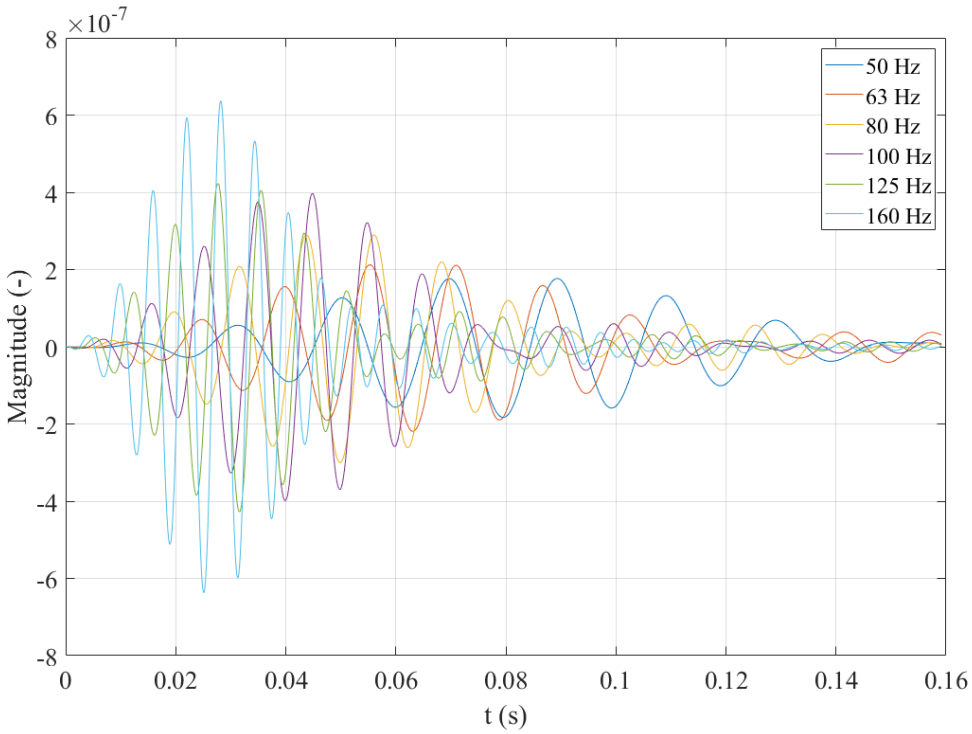

Figure 3.8: The impulse response at a single point from the Comsol model, filter into six third-octave bands.

Figures 3.9 and 3.10 show the backward-integrated impulse responses for several points in the real office building and in the corresponding Comsol model. They are included to visualise how these responses were used in the calculation process described in this section.

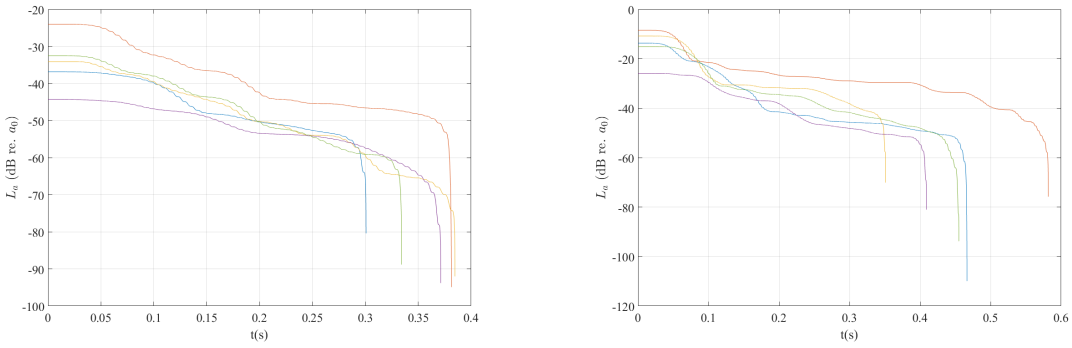

(a) 80 Hz **(b)** 125 Hz

Figure 3.9: Backwards integration impulse curves for selected measured data, from a few different points on the slabs in the office building. The slopes represent reverberation decay for the given frequencies.

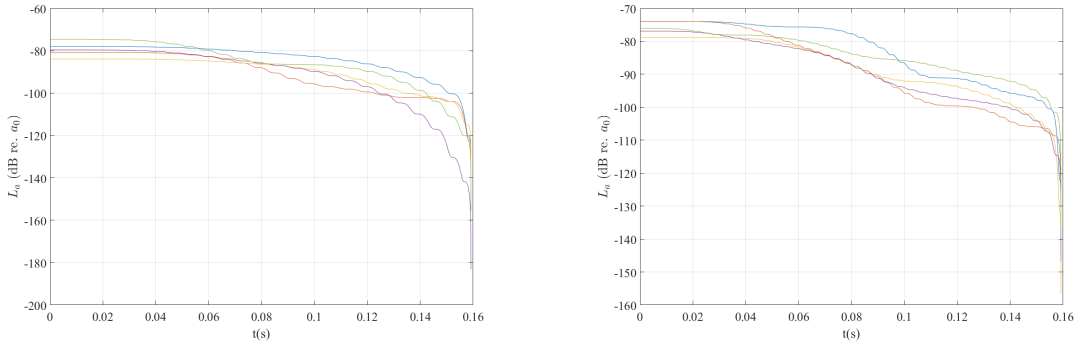

(a) 80 Hz **(b)** 125 Hz

Figure 3.10: Backwards integration impulse curves from Comsol data, from a few different points on the Comsol model. The slope indicates reverberation decay behaviour at two selected frequencies.

The structural reverberation time was then calculated using backward integration curves, as shown in Figures 3.9 and 3.10. Due to insufficient dynamics in the backward-integrated impulse responses, a linear fit was applied to their slopes. The resulting reverberation time was determined as the point where the fitted line dropped by 60 dB from its starting level. This process is illustrated in Figure 3.11 and follows the theory outlined in Section 2.1.

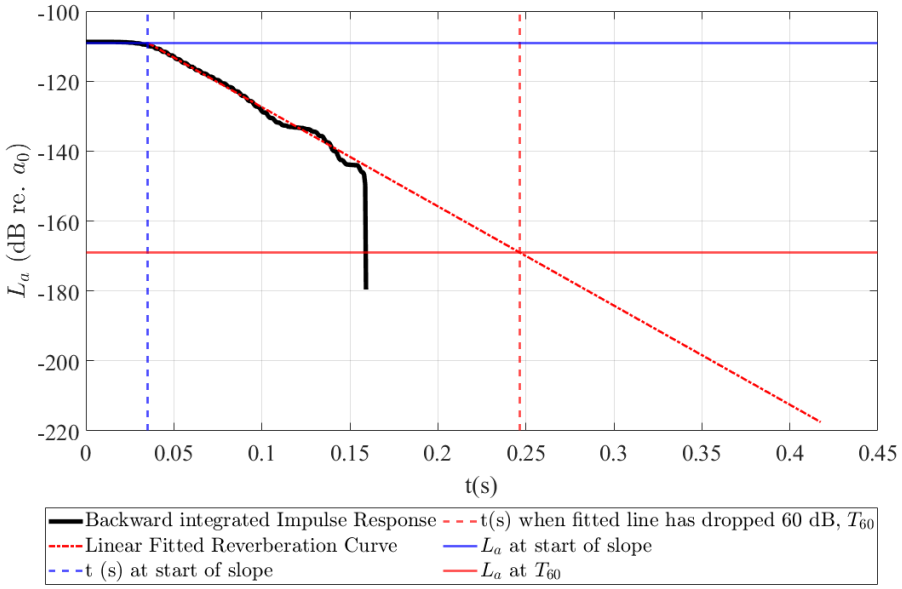

Figure 3.11: Illustrative Figure of the calculation process of the structural reverberation time.

3.4.4 Applications of `fminsearch` and `fitlm` in Matlab and Interpretation of Coefficient of Determination

The Interpretation of the Coefficient of Determination

R-squared (R^2), also known as the coefficient of determination, was a commonly used statistic in the linear regression analyses carried out in this thesis. It described how well the independent variables in a model explained the variation in the dependent variable. R^2 values ranged from 0 to 1 (or 0% to 100%), where a higher value typically indicated a better fit of the model to the data. For example, an R^2 of 0.85 meant that 85% of the variation in the dependent variable was explained by the model.

An important distinction was that $R^2 = 0$ did not necessarily imply that there was no relationship or correlation in the data. Rather, it meant that the fitted model did not capture any of the variance in the dependent variable. For instance, if a linear regression model resulted in $R^2 = 0$, it indicated that the variance in the dependent variable was not explained by a linear trend, although a non-linear relationship might still have existed.

Although a high R^2 was often desirable, it did not automatically mean that the model was good. A model could have a high R^2 while still being biased or poorly specified. Therefore, R^2 was interpreted in combination with plots.

In some cases, especially in the field of engineering, high R^2 values (e.g., > 0.9) were common and expected due to the deterministic nature of the systems. If the goal was to explore relationships between variables, a lower R^2 could still provide useful insights. In summary, R^2 was a useful but incomplete indicator of model fit — knowledge of what was being fitted, and how, remained essential [26].

fminsearch

In the results section, five cases were presented using different variations of an equation to fit parameters to the measured slab data. This fitting process relied on a non-linear solver that searched for local minima, namely `fminsearch` [27].

The expression fitted to the measured data is shown in Equation 3.1, where a was the acceleration at a receiver point, a_0 the acceleration at the excitation point, r the distance from the source, and η a parameter representing internal damping. The factor $1/\sqrt{r}$ accounted for geometrical attenuation:

$$a = a_0 \frac{1}{\sqrt{r}} e^{-\eta r} \tag{3.1}$$

Taking the base-10 logarithm and converting to decibels gave:

$$20 \log_{10}(a) = 20 \log_{10}(a_0) - 10 \log_{10}(r) - \eta\, r\, 20 \log_{10}(e) \tag{3.2}$$

To obtain a general fitting form, the constants were regrouped into three free parameters:

$$20\log_{10}(a) = A - B\,10\log_{10}(r) - C\,r\,20\log_{10}(e) \tag{3.3}$$

Equation 3.3 was implemented in Matlab as a function handle, with A, B, and C as fitting parameters and r (called x in Matlab) as the distance variable. This function was then used to create an objective function minimising the sum of squared errors between the model and the measured slab data:

```
into_fminsearch = @(parameters) ...
    sum((fun_L(parameters, x) - L(:,k)).^2);
```

Here, `fun_L` represented Equation 3.3, and $L(:,k)$ was the measured slab data for each third-octave band. This objective function was passed to `fminsearch`, which estimated the parameters that best fitted the measured data.

The following five fitting cases were formulated and investigated:

- **Case 1**: Geometrical attenuation only — parameters A and B were fitted; $C = 0$.
- **Case 2**: Damping only — parameters A and C were fitted; $B = 0$.
- **Case 3**: All parameters A, B, and C were fitted freely.
- **Case 4**: Cylindrical spreading — B was fixed to 1 ($-10\log_{10} r$); A and C were fitted.
- **Case 5**: Spherical spreading — B was fixed to 2 ($-20\log_{10} r$); A and C were fitted.

This fitting was carried out for third-octave bands between 50–160 Hz. Using the optimal parameters from each case, a new curve was generated and compared to the measured data. The coefficient of determination, R^2, was then calculated for each band to evaluate which case yielded the best fit. The results were summarised using a table template as shown in Table 3.8, where rows contained the values of parameters A, B, and C per frequency band.

Third-octave Band	**50 Hz**	**63 Hz**	**80 Hz**	**100 Hz**	**125 Hz**	**160 Hz**
Parameter A	A_{50}	A_{63}	A_{80}	A_{100}	A_{125}	A_{160}
Parameter B	B_{50}	B_{63}	B_{80}	B_{100}	B_{125}	B_{160}
Parameter C	C_{50}	C_{63}	C_{80}	C_{100}	C_{125}	C_{160}
R^2	R^2_{50}	R^2_{63}	R^2_{80}	R^2_{100}	R^2_{125}	R^2_{160}

Table 3.8: Template table showing how the optimal parameters were presented in the results section.

The effective group velocity, $c_{g,\text{eff}}$, was calculated in two ways. First, using the fitted model, a curve of L_a versus distance was created for each frequency band. The slope dL/dx was extracted at 1 m intervals, and together with the average T_{60} from the measured data, Equation 2.3 was used to estimate $c_{g,\text{eff}}$. Second, $c_{g,\text{eff}}$ was estimated using the centre time t_c according to $c_{g,\text{eff}} = \Delta x/t_c$, where Δx was the distance from the excitation point to the measurement point.

fitlm

The Matlab function `fitlm` was used to perform ordinary least-squares linear regression [28]. It was used to identify trends in the fitted data and to evaluate whether the decay behaviour was primarily linear (suggesting damping-dominated decay) or logarithmic (suggesting geometric spreading). The model fit was assessed using the coefficient of determination R^2. A high R^2 indicated strong agreement with a linear model, while a low R^2 suggested either a logarithmic trend or no clear pattern. All regressions were conducted with the x-axis on a linear scale.

3.4.5 Potential Trouble-shooting

A sufficiently large eigenfrequency search could not be completed to cover the full range of third-octave bands that were investigated. Although there will still be energy present across the entire range, it would have been preferable to include a wider span of eigenfrequencies, up to 240 Hz. However, the computational time was too long to successfully complete such a search. An iterative method was attempted, but it resulted in incomplete phase information for the structure, so the extensive single search was used instead.

4
Results

To address the research question of whether an energy-based model can predict the attenuation of structure-borne vibrations, this chapter presents a detailed analysis of three key quantities: the reverberation time T_{60}, the effective group velocity c_{eff}, and the distance-dependent decay of the vibration level L_a (acceleration level in dB). Unless otherwise specified, all values are derived from the centre of gravity time of the impulse response at each measurement position. Results are presented for the third-octave bands centred at 50 to 160 Hz for floors 3 to 5 of the in-situ measured office building.

All levels represent the vertical (z-axis) component of acceleration, expressed in m/s^2. This corresponds to vibrations perpendicular to the surface of the measured elements. Results for the concrete pillars are provided only in Appendix A.1.2. The rest of the chapter examines the behaviour of slabs and their response to plate-like bending waves. In the figures, the reference level a_0 for L_a is defined as the acceleration at the excitation point, which corresponds to the simulated excitation node in the Comsol model and the shaker position in the in-situ measurements, unless stated otherwise.

4.1 Structural Reverberation Time from In-Situ and Comsol for slabs (Floors 3–5)

When plotting the T_{60} values against distance for all measured points, differences in frequencies are observed across the measurement points on the slab. For the in-situ measurements, the minimum reverberation times for all frequencies fall within an interval of approximately 0.41 to 4.4 seconds. However, for the 80 Hz frequency, the variations are smaller compared to the other third-octave bands. Notably, at 10 meters, the 80 Hz frequency exhibits a reverberation time of 4.6 seconds, which appears to be a potential outlier. Compared to Comsol, the reverberation time for 80 Hz is significantly lower than that of the other third-octave bands, measuring 0.9 seconds.

The reverberation time for both the measured in-situ data as well as for the Comsol data can be seen in Figure 4.1 respectively 4.2. All individual values for each measurement point from the in-situ measurements and the Comsol simulations are presented in Appendix A.1.

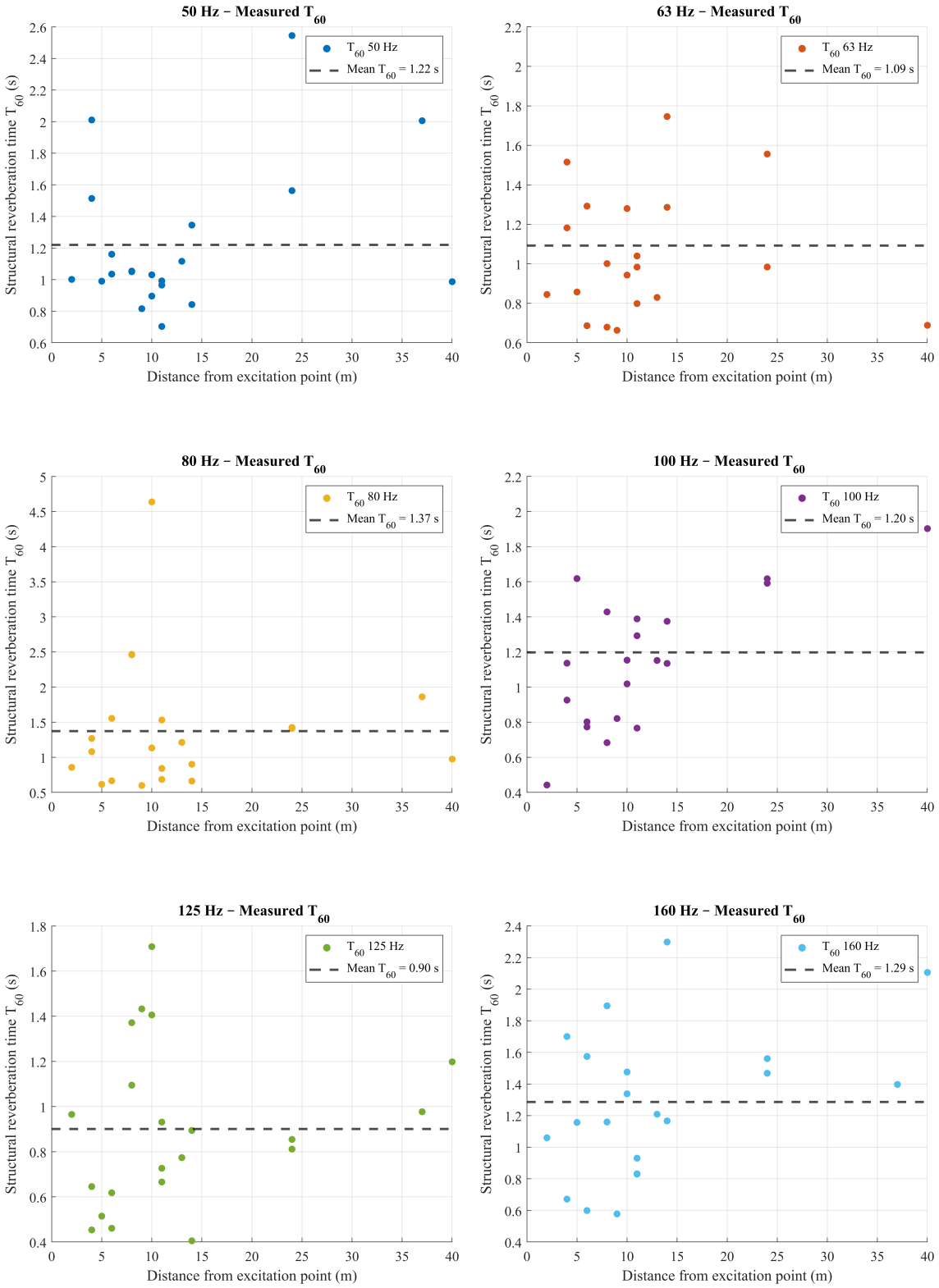

Figure 4.1: The measured reverberation time, T_{60}, across one-third-octave bands based on in-situ measurements.

The T_{60} results from the Comsol simulations indicate that the minimum reverberation time across all frequencies falls within approximately 0.17 to 3.1 seconds. The reverberation time is most closely aligned with the third-octave bands at 50 Hz and 80 Hz, while there is a noticeable difference in reverberation time as the frequency increases. Additionally, there is no distance-dependent variation in the spread of the reverberation time. The variation of the reverberation time over distance could affect the following results when using the mean for the analytical solution for the level decay. It seems like the lowest reverberation time is obtained for 50 Hz with a mean value of 0.29 seconds. This could indicate a higher damping for 50 Hz compared to the other frequencies for the system.

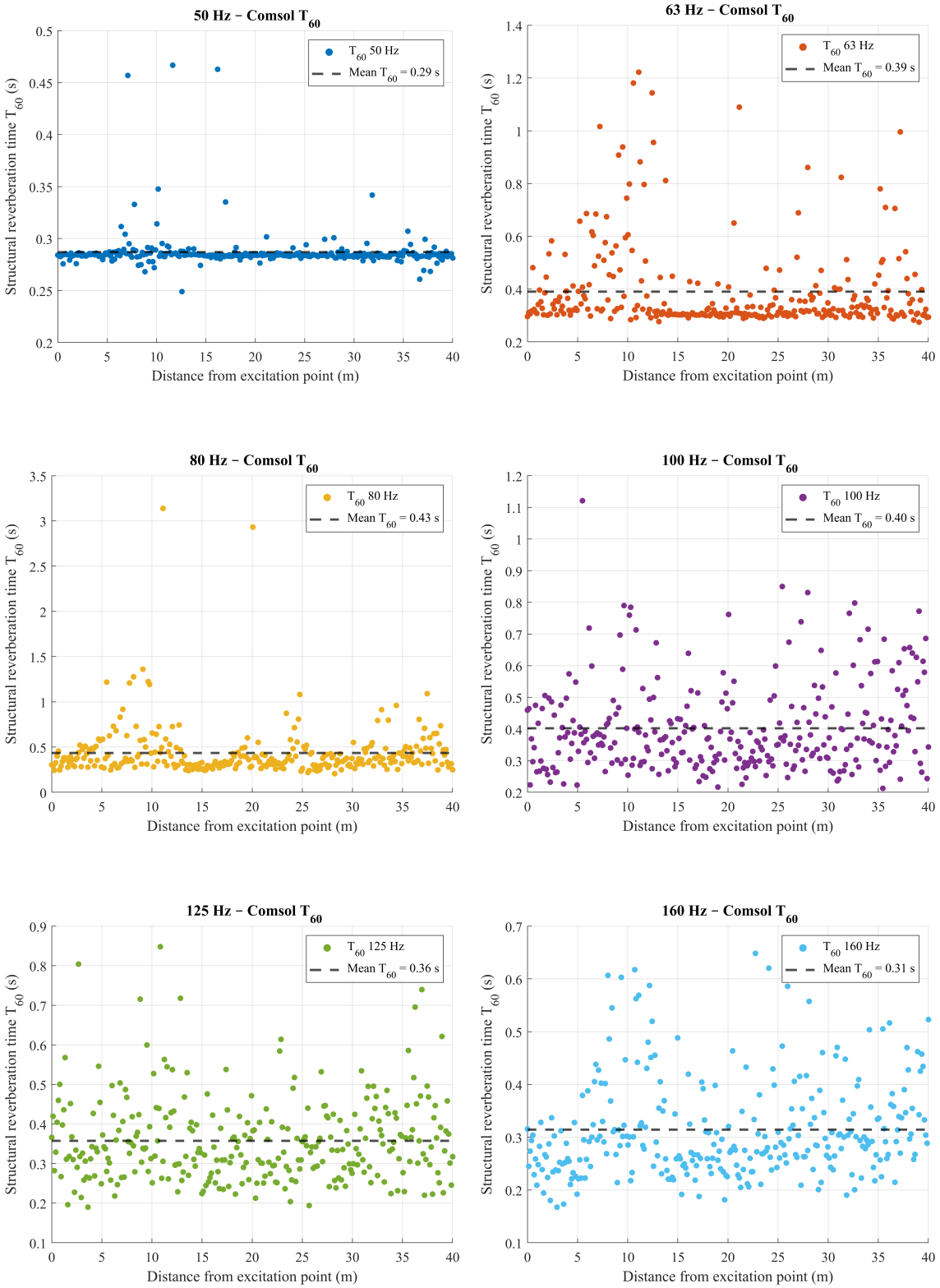

Figure 4.2: Simulated reverberation time, T_{60}, across one-third-octave bands based on Comsol simulations.

The in-situ measurements show significant differences compared to the results from the Comsol simulations, (see Table 4.1). However, the absolute values cannot be

directly compared. The much shorter reverberation times in the simulations may suggest that the system modelled in Comsol is more heavily damped due to the idealised boundary conditions.

Band (Hz)	50	63	80	100	125	160
Measured $\overline{T_{60}}$ (s)	1.22	1.09	1.37	1.20	0.90	1.29
Comsol $\overline{T_{60}}$ (s)	0.29	0.39	0.43	0.40	0.36	0.31
Difference (s)	0.93	0.70	0.94	0.80	0.54	0.98

Table 4.1: Comparison of the average reverberation times, $\overline{T_{60}}$ for in-situ measurements and Comsol simulations across one-third octave bands.

4.2 Analytical Attenuation Curve Fitting of L_a vs. Distance for Five Cases

The parameter fitting of Equation 3.3 to the in-situ measured data using `fminsearch` for the different cases is presented below.

4.2.1 Case 1: Geometrical Attenuation

Table 4.2 has the parameters for case 1 per third-octave band. The resulting curve from the parameters is shown in Figure 4.3. Case 1 only fits a parameter for the starting value, parameter A, and, considering the geometrical attenuation, it is parameter B. The values for parameter B increase linearly with frequency. The R^2 is below 0.5 for all, but increases with frequency.

Third-octave Band	**50 Hz**	**63 Hz**	**80 Hz**	**100 Hz**	**125 Hz**	**160 Hz**
parameter A	-34.618	-25.868	-24.405	-17.857	-3.614	1.334
parameter B	0.855	1.316	1.310	1.401	1.608	1.724
parameter C	-	-	-	-	-	-
R^2	0.192	0.229	0.300	0.342	0.484	0.433

Table 4.2: The parameters from `fminsearch` when fitting for only the geometrical distance attenuation.

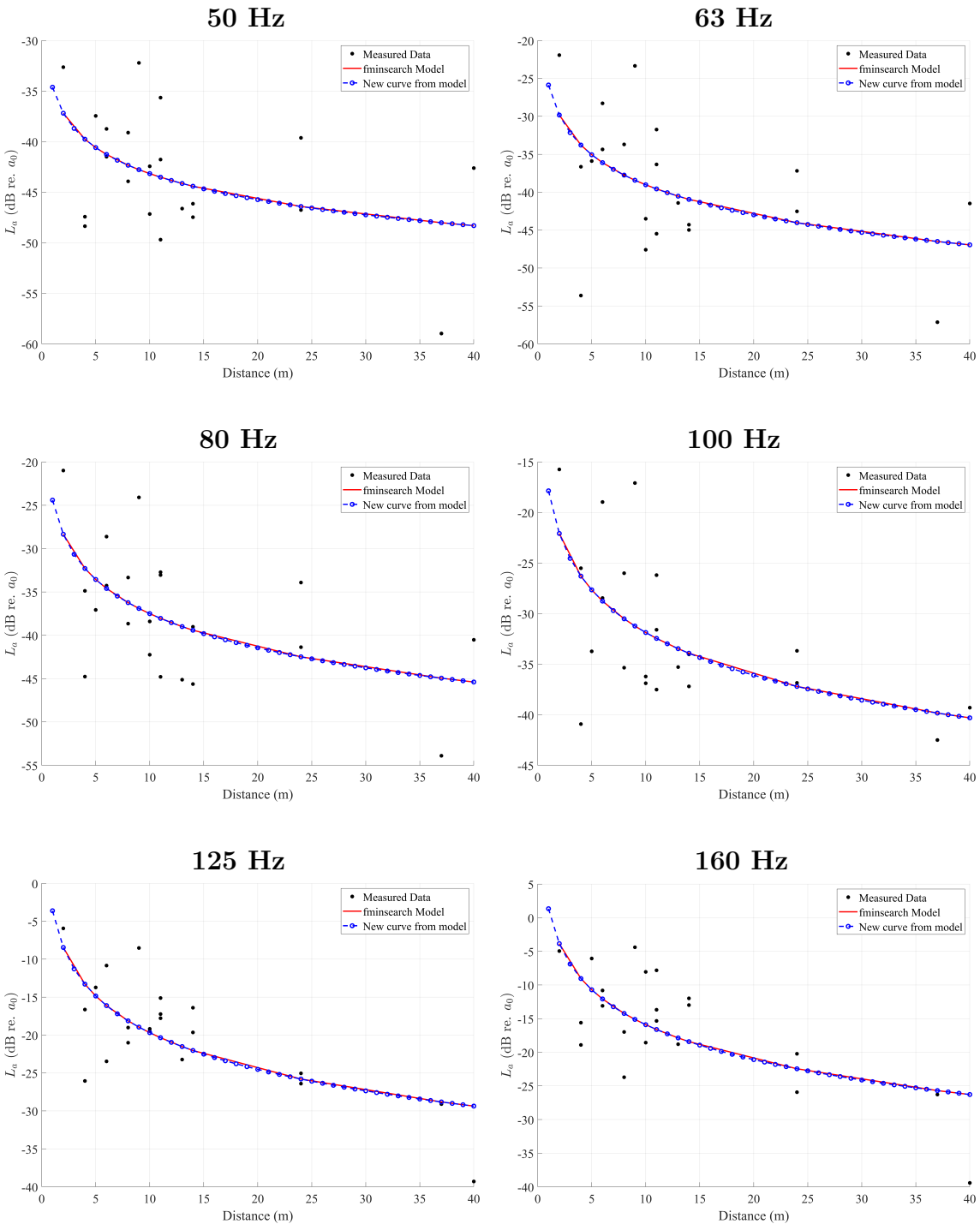

Figure 4.3: The measured data are shown as black dots, and the resulting `fminsearch` model is the red line in the legend. The blue dotted line is a curve fitted with the parameters in Table 4.2. This is all done per third-octave band and repeated for each case.

4.2.2 Case 2: Damping Attenuation

Table 4.3 has the parameters for case 2 per third-octave band. The resulting curve from the parameters is shown in Figure 4.4. Case 2 only fits a parameter for the starting value, parameter A, and for the damping attenuation, parameter C. Here, R^2 is close to 0.6 for 125 Hz and 160 Hz, but low for the other third-octave bands. The trend lines here are linearly decreasing because there is no logarithmic component being fitted.

Third-octave Band	**50 Hz**	**63 Hz**	**80 Hz**	**100 Hz**	**125 Hz**	**160 Hz**
parameter A	-39.780	-34.041	-32.728	-26.709	-12.568	-7.838
parameter B	-	-	-	-	-	-
parameter C	0.060	0.089	0.085	0.092	0.127	0.144
R^2	0.183	0.200	0.243	0.282	0.579	0.579

Table 4.3: The parameters from `fminsearch` with no geometrical distance attenuation, whilst fitting for damping.

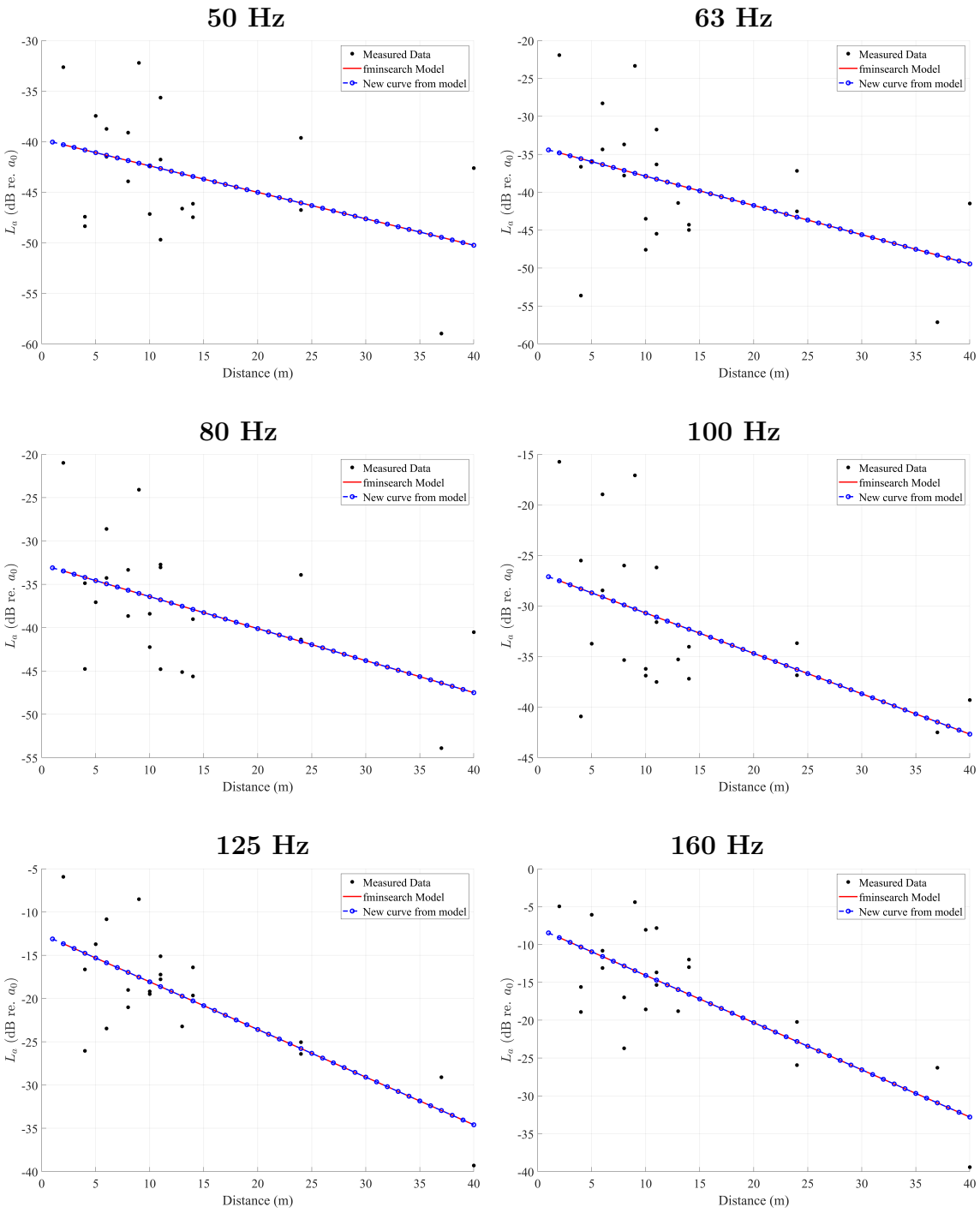

Figure 4.4: The resulting Figures from the parameters from Table 4.3

4.2.3 Case 3: Combined Geometrical and Damping Attenuation

Table 4.4 presents the fitted parameters for Case 2 across third-octave bands. The resulting fitted curves are shown in Figure 4.5. In Case 3, three parameters are fitted: the initial level, parameter A; the geometrical attenuation, parameter B; and the damping attenuation coefficient, parameter C. This model does not assume a predefined spreading geometry (such as cylindrical, $N = 10$, or spherical, $N = 20$). The resulting geometrical attenuation parameters tend to lie closer to 1 than to 2 for several third-octave bands, suggesting a propagation behaviour that trends toward cylindrical spreading. The R^2 values here are, on average, the highest: for 125 Hz and 160 Hz they are close to 0.6, while for the other third-octave bands they are still low, but higher than in the other cases.

Third-octave Band	**50 Hz**	**63 Hz**	**80 Hz**	**100 Hz**	**125 Hz**	**160 Hz**
parameter A	-36.298	-26.724	-23.845	-17.656	-12.545	-11.515
parameter B	0.553	1.162	1.411	1.437	0.004	-0.584
parameter C	0.024	0.012	-0.008	-0.003	0.127	0.182
R^2	0.197	0.230	0.301	0.342	0.579	0.587

Table 4.4: The parameters for Case 3 from `fminsearch`, when fitting for geometrical distance attenuation and damping.

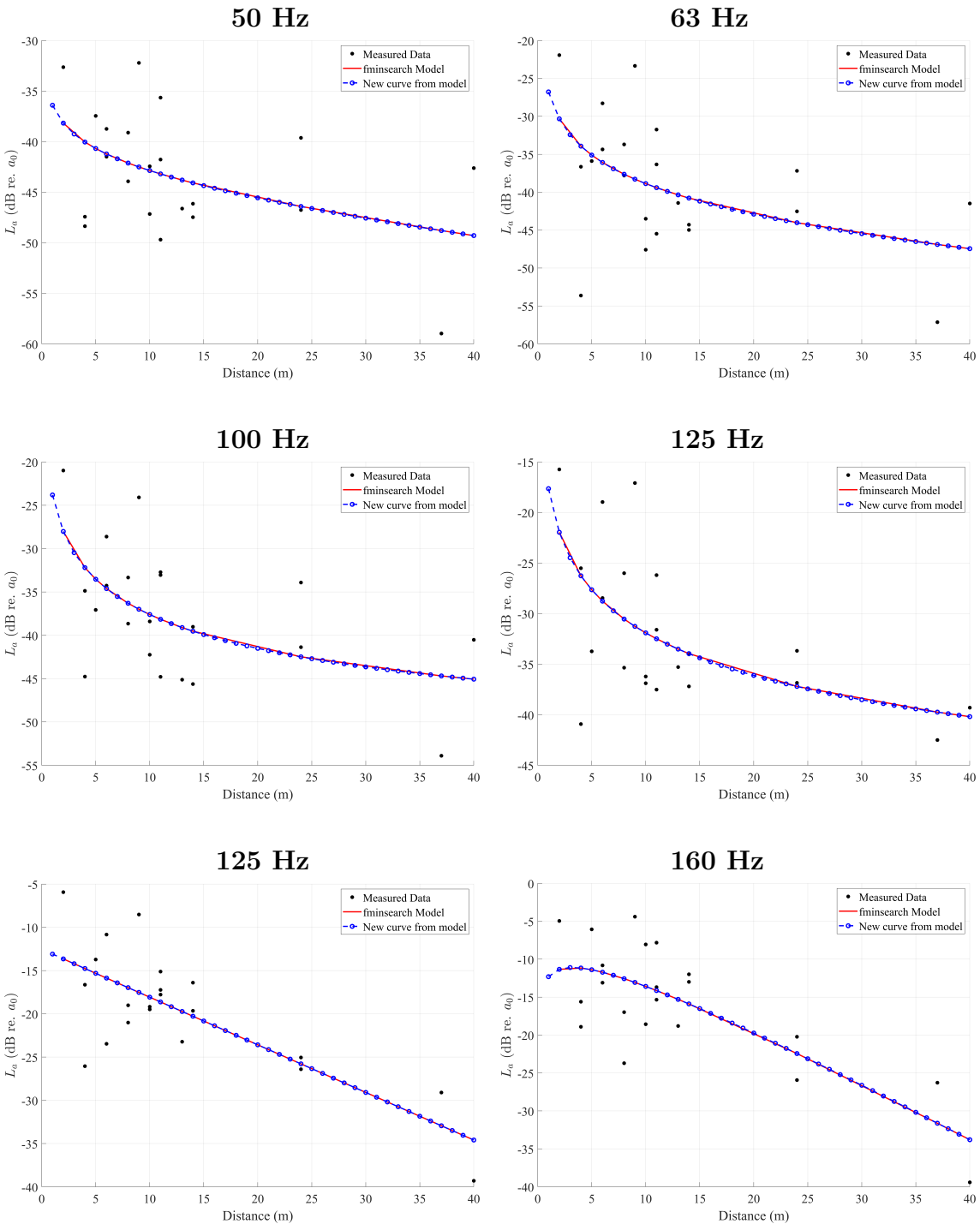

Figure 4.5: The resulting Figures from the parameters from Table 4.4.

4.2.4 Case 4: Cylindrical Geometrical and Damping Attenuation

Table 4.5 has the fitted values for Case 4, which assumes cylindrical geometrical spreading ($N = 10$), represented by parameter B being equal to one for all third-octave bands. The corresponding curves for these parameters can be found in Figure 4.6. The R^2 values here are slightly above 0.5 for 125 Hz and 160 Hz, lower than in Case 3. The remaining R^2 values are also low and tend to increase with frequency.

Third-octave Band	**50 Hz**	**63 Hz**	**80 Hz**	**100 Hz**	**125 Hz**	**160 Hz**
parameter A	-33.482	-27.743	-26.431	-20.411	-6.270	-1.541
parameter B	1	1	1	1	1	1
parameter C	-0.006	0.023	0.019	0.026	0.061	0.078
R^2	0.188	0.229	0.296	0.336	0.548	0.527

Table 4.5: The parameters from `fminsearch` with fixed geometrical distance attenuation ($N = 10$), whilst fitting for damping.

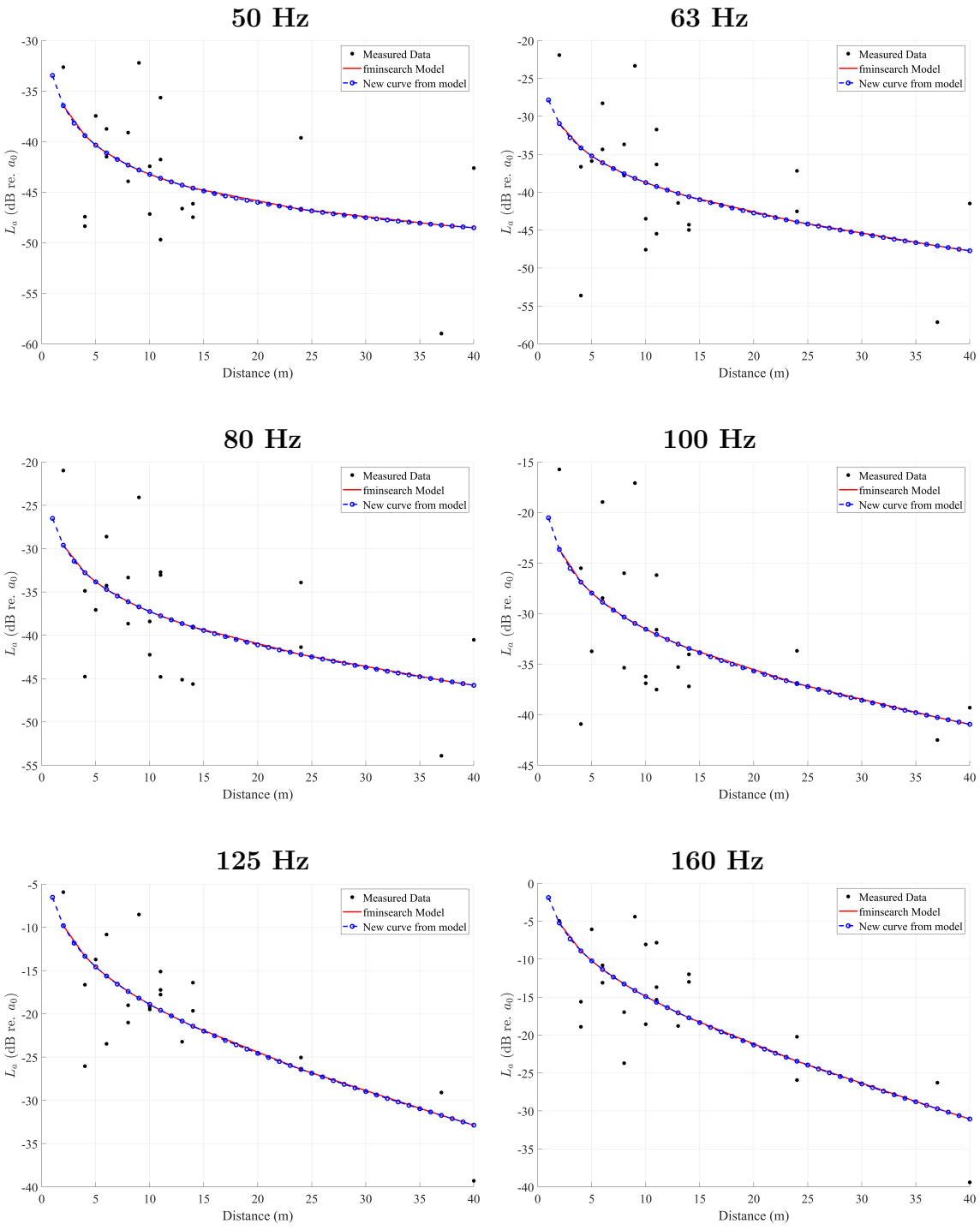

Figure 4.6: The resulting Figures from the parameters from Table 4.5.

4.2.5 Case 5: Spherical Geometrical and Damping Attenuation

Table 4.6 shows the fitted values for Case 5, where spherical geometrical spreading is assumed ($N = 20$), corresponding to parameter $B = 2$ for all third-octave bands.

The fitted curves using these parameters are presented in Figure 4.7. The R^2 values are below 0.5 for 125 Hz and 160 Hz, which are lower compared to Case 3. Overall, the R^2 values remain relatively low, but tend to increase with frequency.

Third-octave Band	**50 Hz**	**63 Hz**	**80 Hz**	**100 Hz**	**125 Hz**	**160 Hz**
parameter A	-27.184	-21.445	-20.133	-14.114	0.028	4.757
parameter B	2	2	2	2	2	2
parameter C	-0.072	-0.043	-0.047	-0.040	-0.005	0.012
R^2	0.106	0.215	0.291	0.333	0.456	0.426

Table 4.6: The parameters from `fminsearch` with fixed geometrical distance attenuation ($N = 20$), whilst fitting for damping.

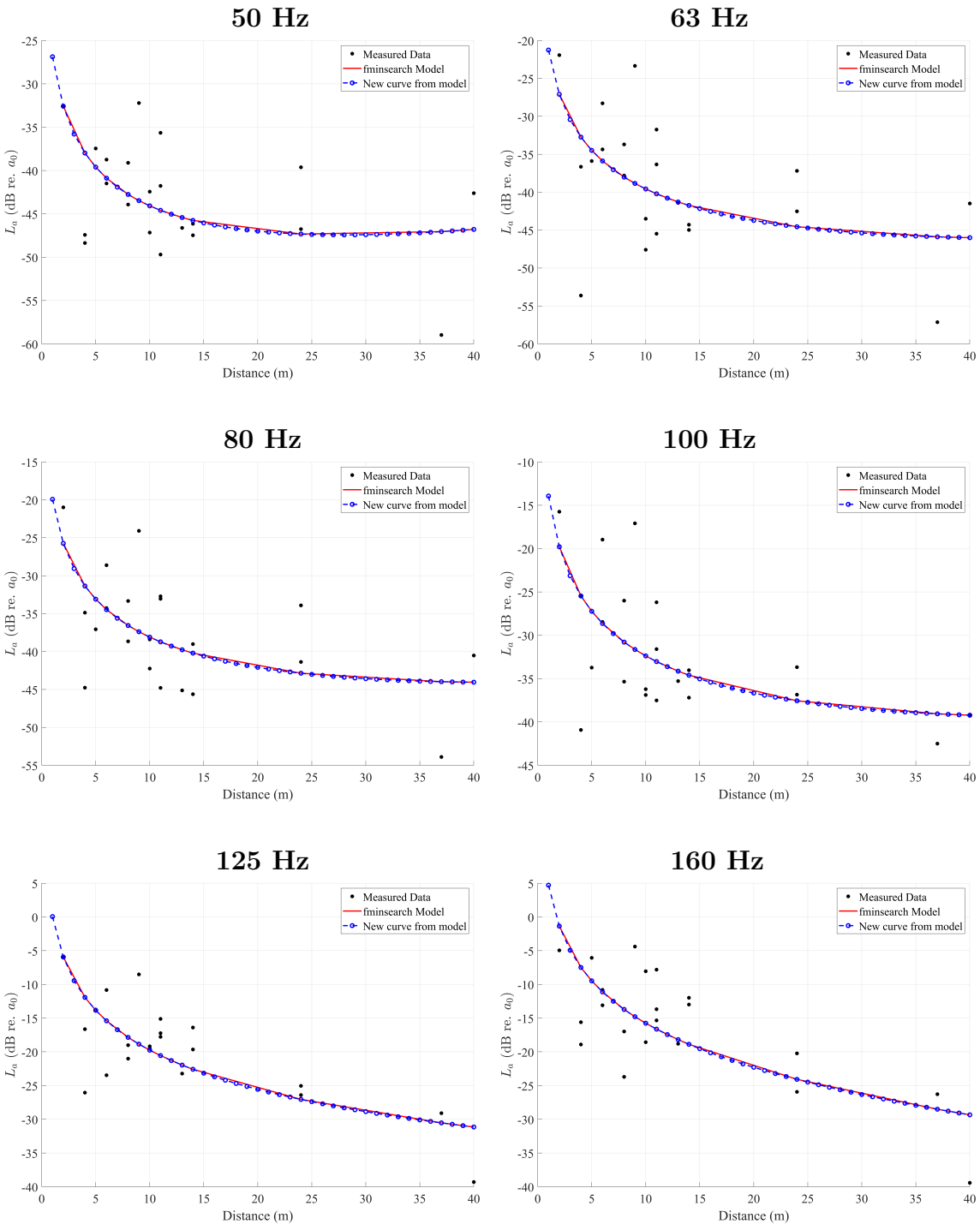

Figure 4.7: The resulting Figures from the parameters from Table 4.6.

General trends for all cases are that the calculated R^2 increases with frequency. They all exhibit curve patterns similar to the curves found in Figure 4.8, except Case 2, where the attenuation trend appears linear. The highest R^2 values are found in Case 2, Case 3, and Case 4, with Case 3 being the highest. This suggests that the investigated system aligns with Case 3, involving cylindrical geometrical spreading and damping, which is examined further in the following Sections.

4.2.6 Theoretical Optimisation Model Based on Building Parameters

The analytical expression in Equation 2.16, which includes both geometrical spreading and material damping, is illustrated in Figure 4.8. The model uses the same material parameters as those listed in Table 3.1 for the slab at the office building.

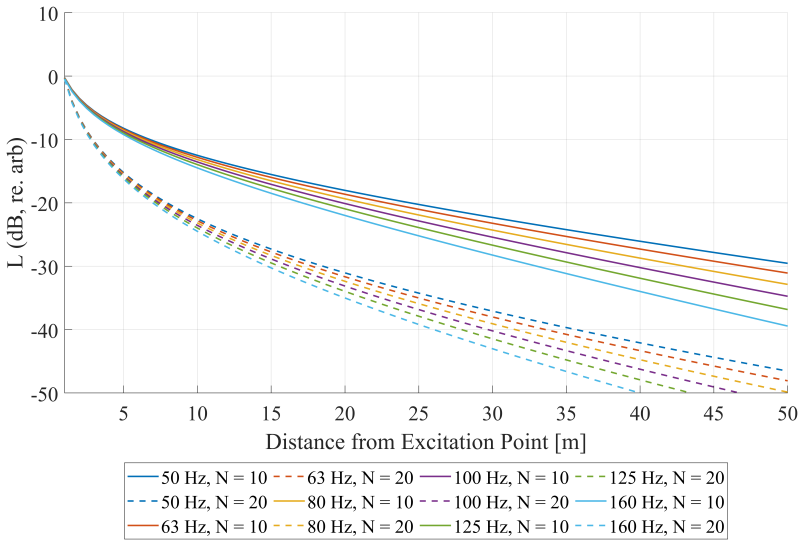

Figure 4.8: The level attenuation for the theoretical slab model across distances. The solid and dashed lines represent fitted trends for cylindrical ($N = 10$) and spherical ($N = 20$) attenuation, respectively.

To be able to compare with the five cases presented earlier in Section 4.2, a `fminsearch` analysis was also conducted on the analytically generated data and can be seen in Table 4.7, and the final analysis presented in the table is limited to the case of cylindrical spreading with damping ($N = 10$), as this was the scenario found to best align with the measured slab data for the office.

When comparing Table 4.7 to the results from Cases 1 to 5, it can be seen that the fitted damping parameter C is higher for the analytical case. The geometrical spreading parameter B remains fixed at 1, and A stays close to 0, which is consistent with expectations for this model. The trend in Figure 4.8 confirms that the energy decay is less pronounced for cylindrical spreading compared to spherical spreading.

Third-octave Band	**50 Hz**	**63 Hz**	**80 Hz**	**100 Hz**	**125 Hz**	**160 Hz**
parameter A	-0.00080	0.00161	0.00075	0.00061	0.00269	0.00038
parameter B	1.00010	1.00015	1.00006	1.00005	1.00029	1.00002
parameter C	0.25084	0.28157	0.31731	0.35476	0.39659	0.44875

Table 4.7: Optimised `fminsearch` parameters for each third-octave band, assuming full distance-based attenuation with fixed $N = 10$.

4.2.7 Using Cylindrical Geometrical Spreading and Damping Based on $\overline{T_{60}}$ from Measured and Comsol Simulation Data

The analytical solution for the geometrical and internal energy loss for the magnitude of L_a is shown in Figure 4.9.

Figure 4.10 is based on values obtained by analysing the real structure and the simulated structure's FRF, retrieving η based on the value of $\overline{T_{60}}$ and the distances used between the measurement points and the excitation point.

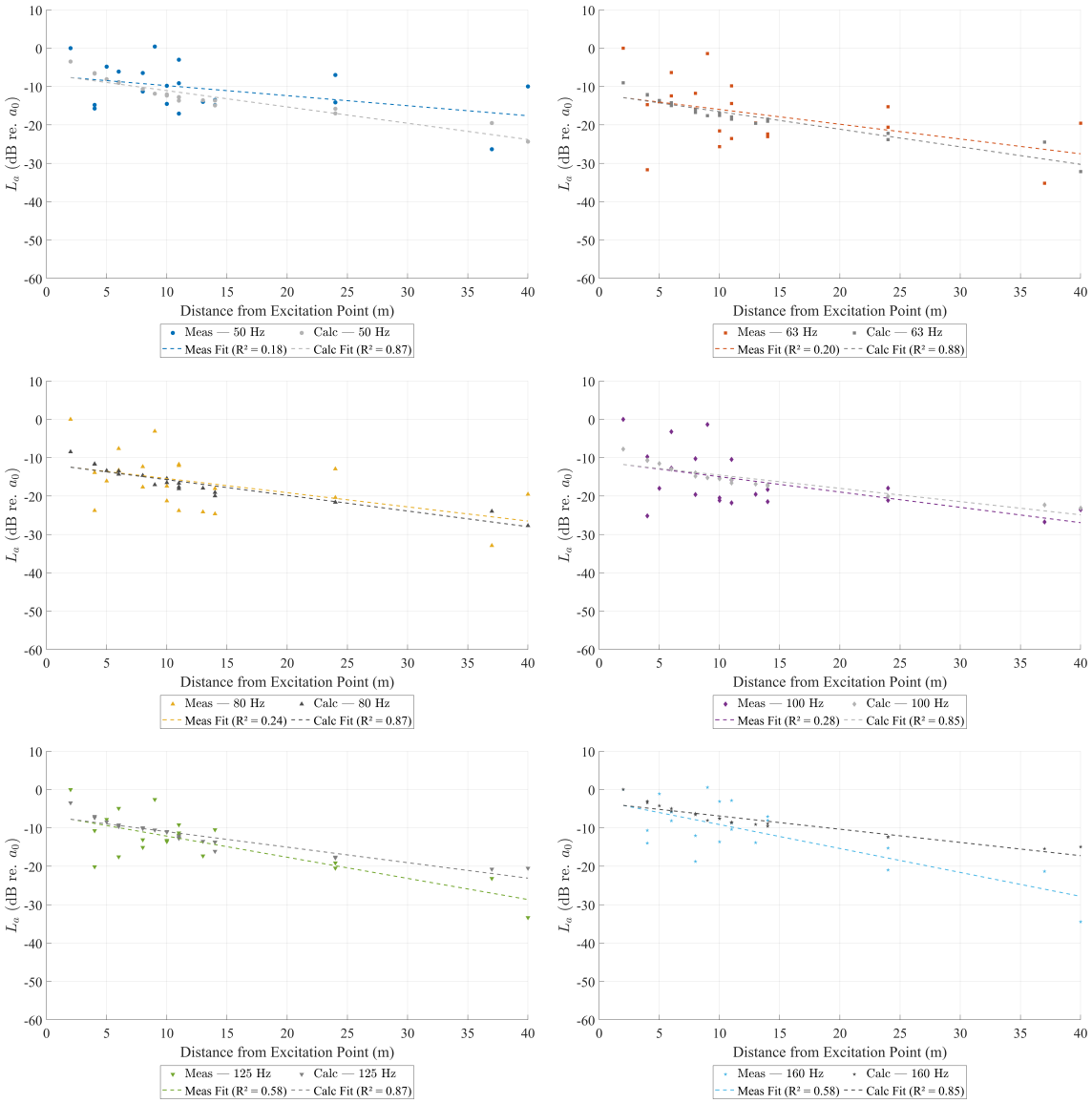

Figure 4.9: The level attenuation for the measured slab result. The dotted lines are fitted trends with their R^2-value. The top left to bottom right shows the third-octave bands 50 Hz to 160 Hz. The dark-coloured lines and dots represent Equation 2.15; the coloured lines and dots represent the original measured slab data. The reference a_0 is defined as the acceleration at the point nearest to the excitation point.

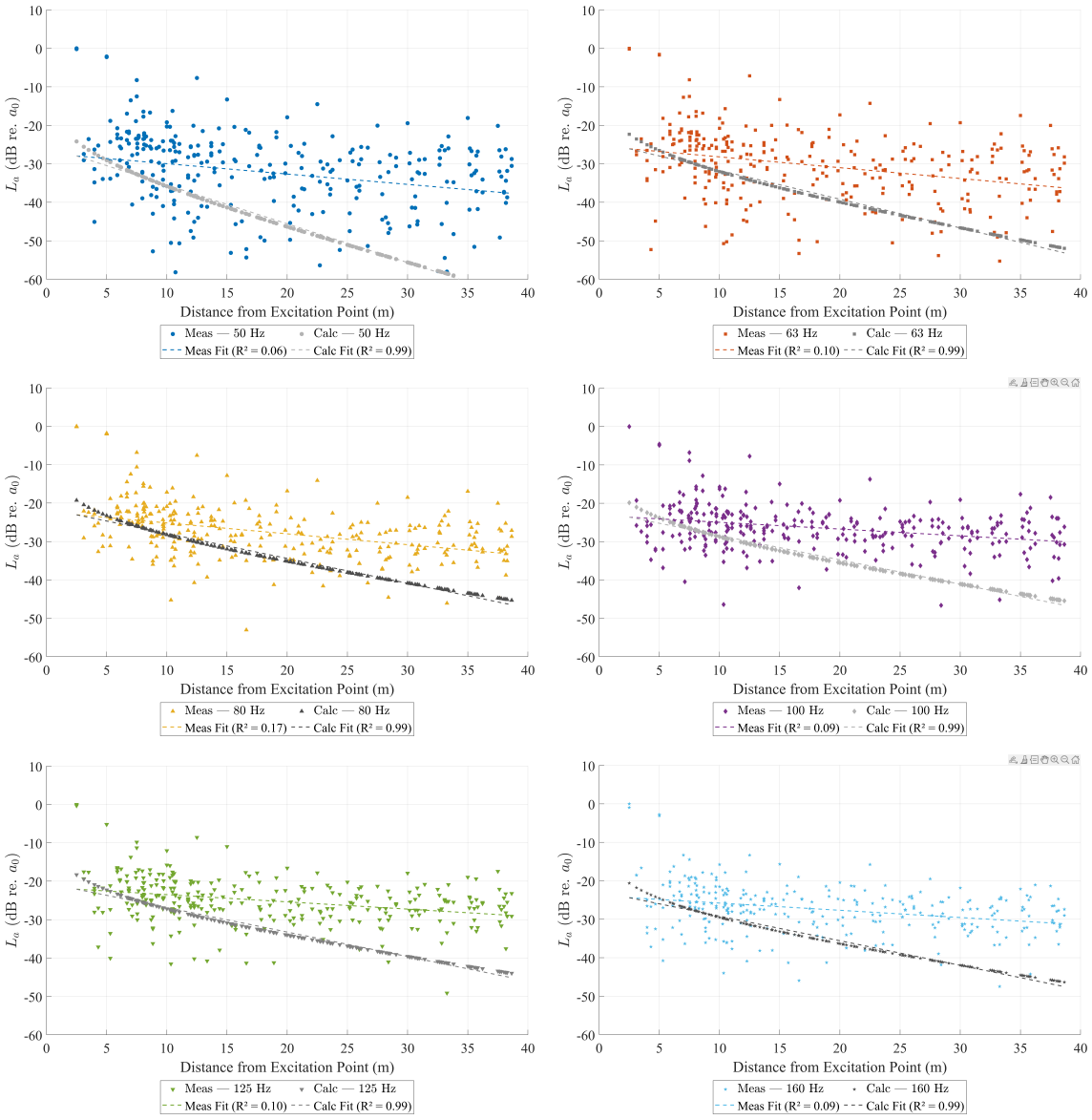

Figure 4.10: The level attenuation for the Comsol slab result. The dotted lines are fitted trends with their R^2-value. Top left to bottom right shows the third-octave bands 50 Hz to 160 Hz. The dark-coloured lines and dots represent Equation 2.16; the coloured lines and dots represent the original Comsol slab data. The reference a_0 is defined as the acceleration at the point nearest to the excitation point.

Comparing the results in Figures 4.9 and 4.10, based on how well they align with Equation 2.15—which was found to best fit Case 4 in Section 4.1—shows that the Comsol data deviate more from the fitted Equation 2.15 than the measured data do. The Comsol data's linear fit differs by about 20 dB for all third-octave bands, whilst the measured data's linear fit varies more but at most differs by 10 dB, and in some cases aligns well and differs almost not at all. This indicates that Case 4 is most likely not the best fit for the Comsol data, and that it might correspond to a different attenuation case.

4.2.8 The Estimated Time Delay $\triangle t$ - for the simulations in Comsol and the In-Situ measurements

The calculated time delay based on the estimated centre time of gravity t_c for the in-situ measurement aligns somewhat with the hypothesis predicting a delay over distance. As shown in Figure 4.11, the time delay increases for all trendlines across the investigated frequencies. However, the R^2 ranges from 0.01 to 0.28, indicating a weak linear relationship between distance and the increase in time delay $\triangle t$.

The time delays observed for the measuring points derived from the modal analysis through Comsol simulations show no time delay at 50 Hz, which may indicate a calculation error. In contrast, other frequencies display varying time delays over distance. The most significant time delays are evident between 100 Hz and 160 Hz, while the frequencies of 63 Hz and 80 Hz show almost no increase in time delay over distance. For the trendlines concerning the simulations, the R^2 is also low, ranging from 0 to 0.08, indicating a weak linear relationship between distance and the increase in time delay $\triangle t$.

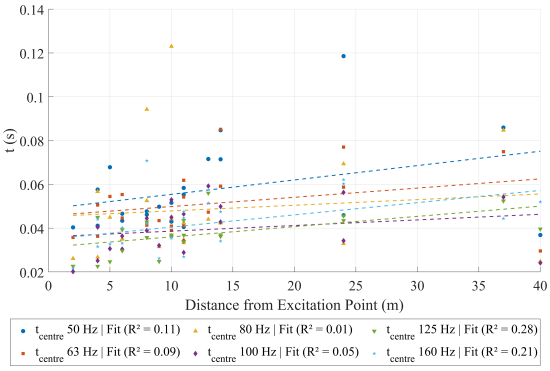

Figure 4.11: Time delay calculated using the centre time t_c from in-situ measurements (all floors combined, slabs).

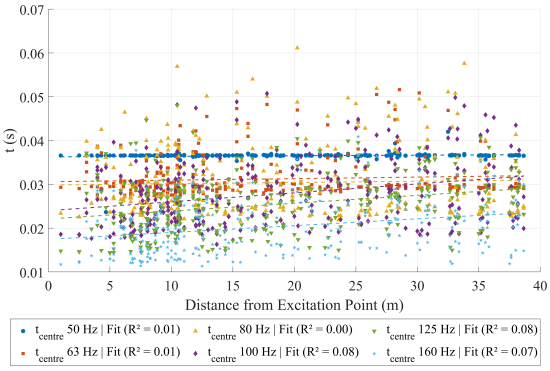

Figure 4.12: Time delay calculated using the centre time t_c from Comsol simulations (all floors combined, slabs).

4.3 Decay of Vibrational Level L_a Over Distance – Comparison Between Comsol Simulation and In-Situ Measurements.

As described in the background, identifying a connection between the reverberation time and the time delay ($\triangle t$) can be used together to predict if there is a proportionality between the reverberation time and the vibrational level decay across distance L_a in concrete structures. This chapter presents the results on level decay over distance, using both Comsol simulations and in-situ measurements. In addition, the centre time of gravity t_c is used as an indicator of the transition from the direct field to the reverberant field, enabling an estimate of time-based propagation characteristics. Only the results for slabs are presented here. Both slab and pillar measurements and simulations were performed, but the main focus is on plate be-

haviour. The results of the pillars can therefore be seen in the appendix in Figure A.1 for the in-situ measurement and Comsol in Figure A.5.

4.3.1 Vibrational Level Over Distance for L_a on Floors 3 to 5, Based on In-Situ Measurements

The in-situ results for vibrational level L_a indicate a general decay with distance across floors 3, 4, and 5. For all investigated frequency bands, the trend shows a non-linear pattern in the near field (up to approximately 15 metres from the excitation point). Beyond this range, the decay aligns more closely with the linear fits, suggesting that energy losses due to material damping become more dominant at greater distances.

The coefficient of determination R^2 for the fitted regressions ranges from 0.05 to 0.86. This wide span suggests that a single linear model does not fully capture the decay behaviour across all floors and frequencies. In cases where $R^2 < 0.5$.

It should also be noted that the measurement points are more densely spaced at shorter distances, which may bias the linear fit and limit interpretability. Furthermore, the absolute vibrational levels L_a vary between floors. For frequencies from 100 Hz to 160 Hz, floor 5 often shows higher vibrational levels over distance than floors 3 and 4, as can be seen when studying the trend-lines. At lower frequencies (50–80 Hz), this variation is limited to the first 10 metres. See Figure 4.13.

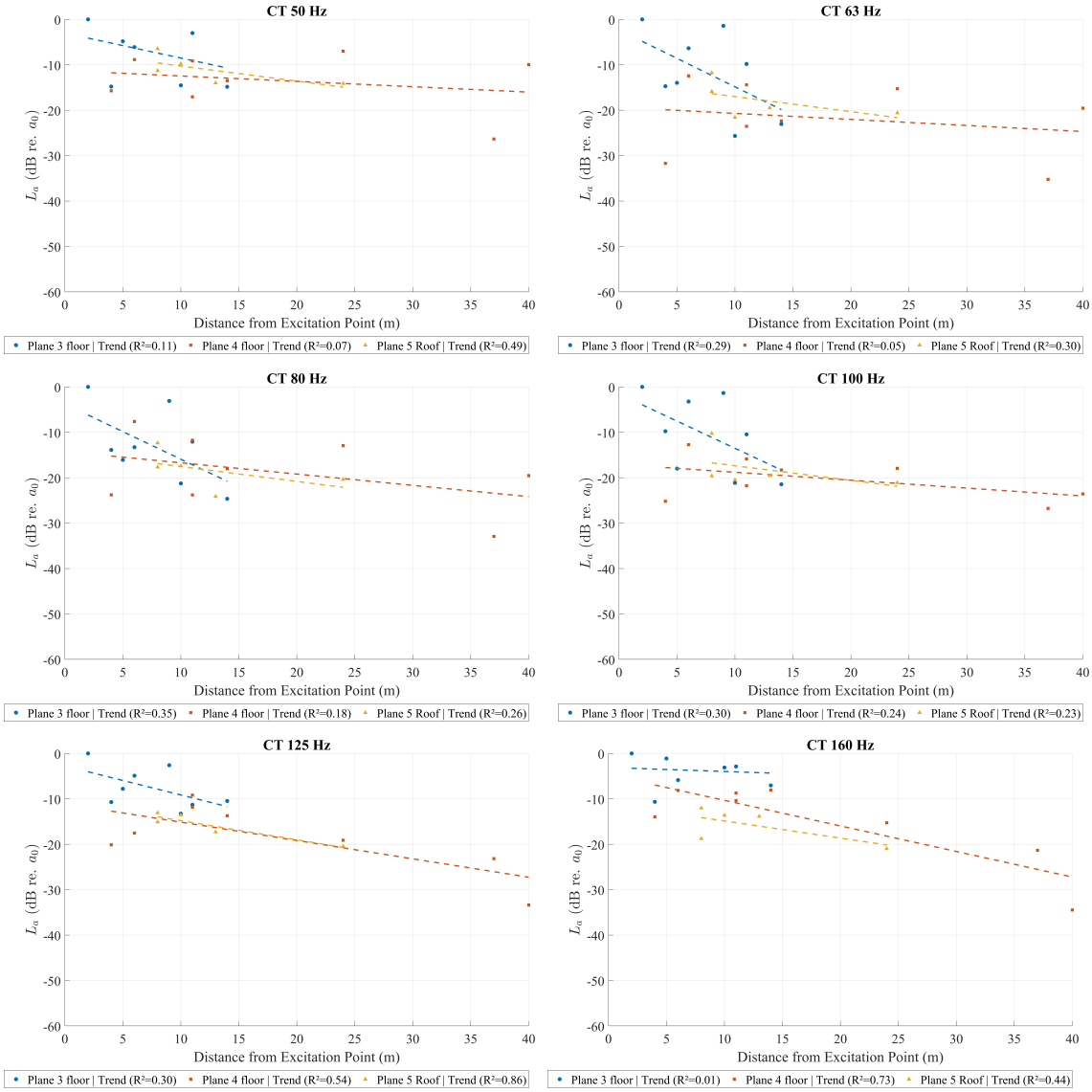

Figure 4.13: The level attenuation for the measured slab result. The dotted lines are fitted trends with their R^2 value. The top left to bottom right shows the third-octave bands 50 Hz to 160 Hz. The reference a_0 is defined as the acceleration at the point nearest to the excitation point.

4.3.2 Vibrational Level Over Distance for L_a floor 3–5 for the simulated Comsol Data

The simulated results from Comsol similarly show a decrease in L_a with increasing distance across all floors and one-third octave bands. However, the linear regression fits for these results yielded low R^2 values, ranging from 0.02 to 0.24, indicating weak linear correlation in decay behaviour.

This suggests that in the simulations, vibrational energy is primarily attenuated due to geometrical spreading rather than damping. This is consistent with idealised simulation models, which may lack the material damping or boundary effects present

in real structures.

As in the measurements, floor 3 consistently exhibits the highest L_a values across most frequency bands and distances. However, at 63–100 Hz, an arbitrary variation is observed, with floor 5 occasionally showing higher levels than the excited floor 3. At lower (50 Hz) and higher (125–160 Hz) frequencies, this variation is mainly observed within the first 10 metres. See Figure 4.14.

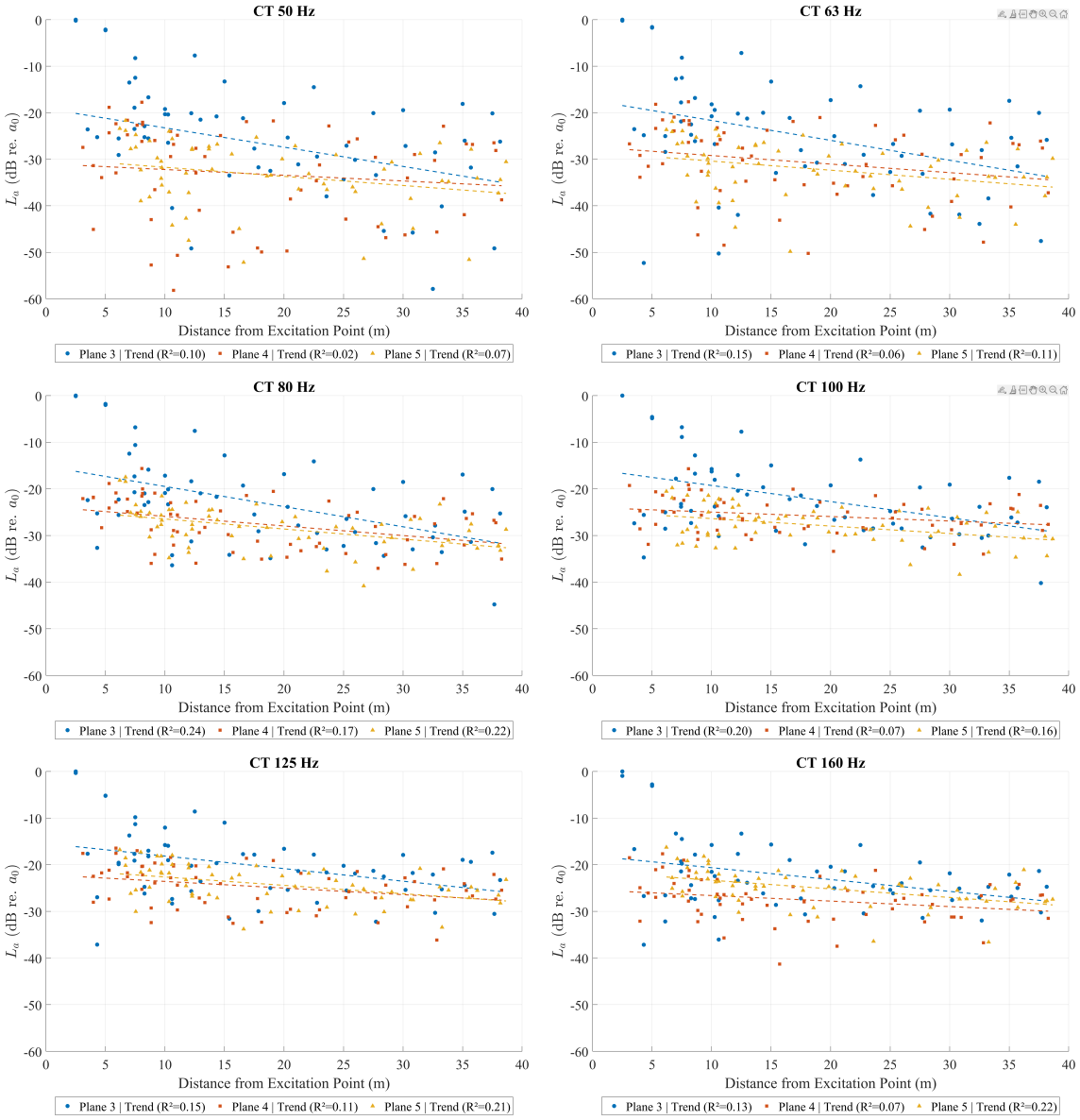

Figure 4.14: The level attenuation for the simulated Comsol result. The dotted lines are fitted trends with their R^2-value. The top left to bottom right shows the third-octave bands 50 Hz to 160 Hz. CT stand for the centre time method used to calculate L_a. The reference a_0 is defined as the acceleration at the point nearest to the excitation point.

A consistent difference of approximately 5 to 20 dB is observed between the simulated Comsol and measured levels across all floor levels when the distance to the source is short, at 5 metres. At longer distances, the results from the simulations and the measurements tend to converge, becoming more similar from 25 metres and beyond, reaching an L_a between -10 and -30 dB.

4.3.3 Effective Group Velocity $c_{\mathrm{g,eff}}$ — Estimated Either Directly from the Centre Time t_c or Analytically Fitted Using `fminsearch`, per Third-Octave Band

Five fitting cases were evaluated in Section 4.2 to determine whether geometric attenuation or energy losses due to damping dominate across the slabs in the system and best describe the propagation of structure-borne waves in the in-situ measurement.

Cases 3 and 4 demonstrated the best fit, yielding the highest R^2 values and providing a visual fit across all third-octave bands. The estimates of $c_{\mathrm{g,eff}}$, derived from the time delay and the actual original data, are presented in Figure 4.15 for the in-situ measurements and in Figure 4.19 for the Comsol simulations.

In particular, case 4 (cylindrical spreading with damping, $N = 10$) showed a consistent fit across third-octave bands, with higher R^2 values and smoother trend lines. This supports the assumption that structure-borne wave propagation in the slabs follows a cylindrical spreading, together with energy losses due to material damping. An increasing trend in estimated $c_{g,\mathrm{eff}}$ with distance was also observed.

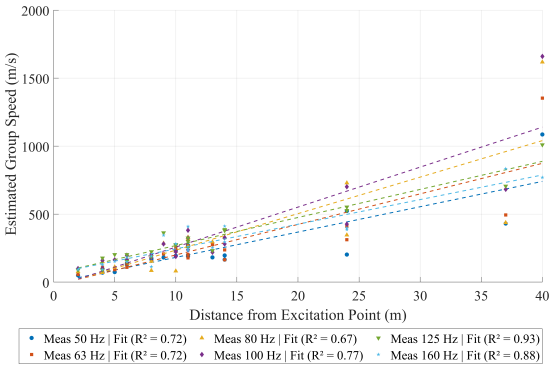

Figure 4.15: Estimated group velocity from centre time t_c based on in-situ measurements on the slabs. Dashed lines indicate linear fits with R^2 values.

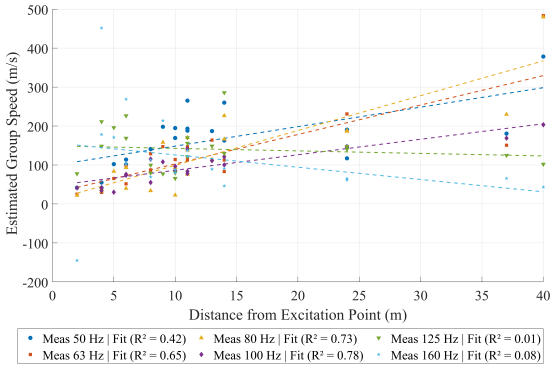

Figure 4.16: Estimated group velocity using `fminsearch` for Case 3, based on in-situ measurements on the slabs.

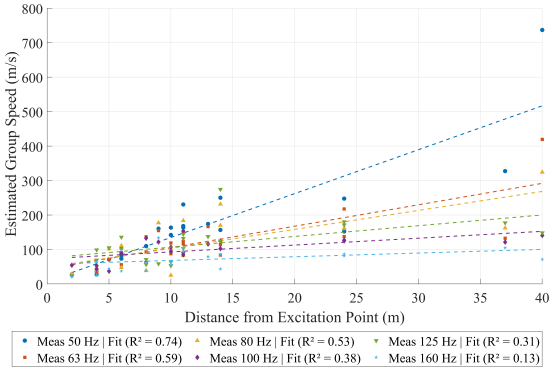

Figure 4.17: Estimated group velocity using `fminsearch` for Case 4, based on in-situ measurements on the slabs.

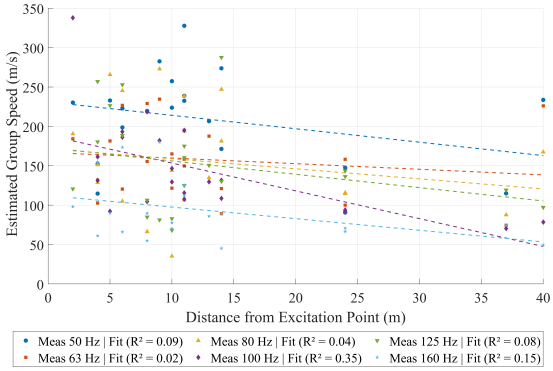

Figure 4.18: Estimated group velocity using `fminsearch` for Case 2, based on in-situ measurements on the slabs.

The group velocity estimated from the simulations using the centre time method t_c, illustrated in Figure 4.19, shows a similar trend to the in-situ results, with increasing $c_{g,\text{eff}}$ across distance and frequency.

When comparing the estimated group velocity from the simulations based on t_c with the fitted results from the analytical models, Case 4 in Figure 4.21 showed the best agreement. This aligns with the findings from the in-situ measurements.

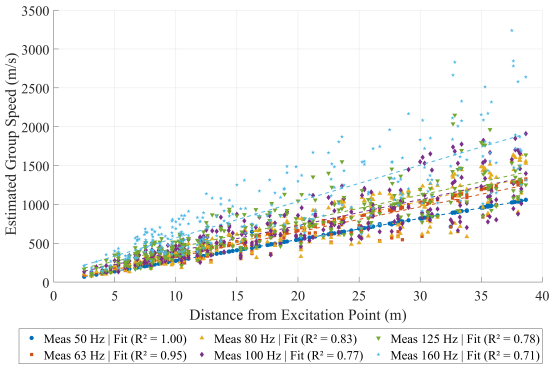

Figure 4.19: Estimated group velocity from centre time t_c, based on Comsol simulations of the slabs.

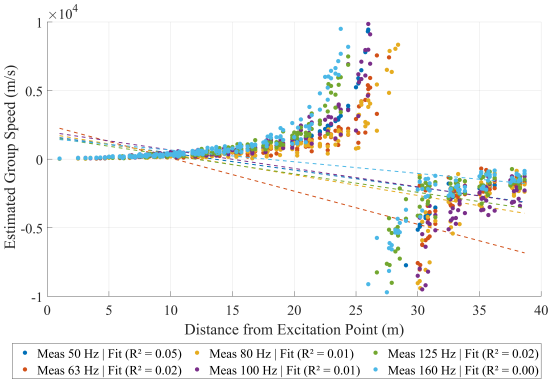

Figure 4.20: Estimated group velocity using *fminsearch* for Case 3, based on Comsol simulations of the slabs.

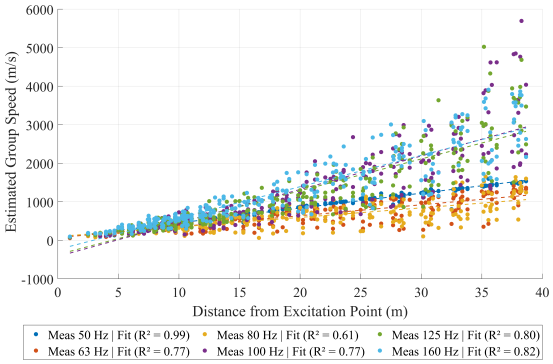

Figure 4.21: Estimated group velocity using *fminsearch* for Case 4, based on Comsol simulations of the slabs.

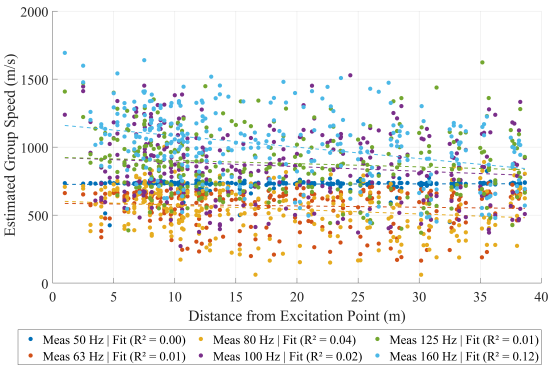

Figure 4.22: Estimated group velocity using *fminsearch* for Case 2, based on Comsol simulations of the slabs.

4.4 Proportionality Between $\overline{T_{60}}$, Distance Attenuation L_a per distance, and Effective Group velocity $c_{\mathrm{g,eff}}$

In Table 4.8 and Table 4.9, a comparison is made between $\overline{T_{60}}$ and the vibrational level L_a per meter obtained from the linear fits of the measurement data in Figure 4.9 and the data from simulations in Figure 4.10. The case 4 based slope values in m/s are derived from the measurement data shown in Figure 4.17 and the Comsol data in Figure 4.21. The centre-time-based group velocity slopes are taken from the linear fits of the measurement data in Figure 4.15 and the Comsol data in Figure 4.19.

No proportional relationship is observed in Table 4.8 between the average reverberation time $\overline{T_{60}}$ and the distance attenuation L_a per meter. While attenuation generally increases with frequency—as expected—no similar dB/m trend is found for $\overline{T_{60}}$.

In Case 4, an inverse trend is evident: the fitted group velocity slope decreases with frequency, whereas the attenuation slope of L_a per meter increases. The centre-time-based group velocity slope increases up to 100 Hz and then decreases beyond that.

The highest and lowest values of $\overline{T_{60}}$ occur at 80 Hz and 125 Hz, respectively.

Third-octave Bands	**50 Hz**	**63 Hz**	**80 Hz**	**100 Hz**	**125 Hz**	**160 Hz**
$\overline{T_{60}}$ **(dB/s)**	1.2202	1.0928	1.3732	1.1972	0.9003	1.2858
L_a **per distance (dB/m)**	-0.2617	-0.3853	-0.3693	-0.3991	-0.5508	-0.6240
Case 4 - analytical $c_{\text{g,eff}}$ **(m/s)**	12.7296	6.2183	5.5093	1.9913	3.1132	1.0696
Centre Time Slope $c_{\text{g,eff}}$ **(m/s)**	18.6280	22.4586	26.8470	29.4113	20.6377	18.1140

Table 4.8: The $\overline{T_{60}}$ for the measured slab data and the slope value of a linear fit (the k in y=kx+m) for the L_a per distance. versus distance in meter (from Figure 4.9), the slope value for the `case 4` effective group velocity estimate (from Figure 4.17), and the effective group velocity estimated using centre time, from Figure 4.11.

In Table 4.9, no discernible trend is observed for $\overline{T_{60}}$, nor is there a clear proportionality between distance attenuation L_a per meter and $\overline{T_{60}}$. In Case 4, the fitted group velocity slope increases with frequency, whereas the attenuation slope of L_a per distance decreases, indicating an inverse relationship. Similarly, the slope of the centre time-based group velocity also increases with frequency, and likewise shows an inverse relationship with the attenuation slope.

Third-octave Bands	**50 Hz**	**63 Hz**	**80 Hz**	**100 Hz**	**125 Hz**	**160 Hz**
$\overline{T_{60}}$ **(dB/s)**	0.2880	0.3871	0.4342	0.3983	0.3585	0.3151
L_a **per distance (dB/m)**	-0.2871	-0.2985	-0.2993	-0.1927	-0.2031	-0.2021
Case 4 - analytical $c_{\text{g,eff}}$ **(m/s)**	38.5451	28.4128	24.7606	86.9246	82.7163	81.5046
Centre Time Slope $c_{\text{g,eff}}$ **(m/s)**	27.2248	32.5218	35.5574	33.9703	34.9109	46.1422

Table 4.9: The $\overline{T_{60}}$ for the Comsol slab data and the slope value of a linear fit (the k in y=kx+m) for the L_a (dB) versus distance in meter (from Figure 4.10), the slope value for the `Case 4` group velocity estimate (from Figure 4.21), and the group velocity estimated using centre time, from Figure 4.12.

The values in Tables 4.8 and 4.9 show no clear proportionality between the vibrational level L_a per meter and the average reverberation time, $\overline{T_{60}}$. However, there appears to be an inverse relationship between the attenuation slopes and the group velocity slopes within both the measurement and Comsol data sets. Interestingly,

the direction of this relationship is reversed when comparing the measurement results to those from the simulations.

5
Discussion

As outlined in the background of this work, the study was motivated by the analogy with room acoustics and the potential for similar vibrational behaviour in wave propagation through structures. The investigation explored the idea of using the reverberation time to predict the spatial level decay over distance in a building.

Even though the results do not fully confirm a quantitative link — neither for the in-situ measurements nor for the Comsol simulations — across all measurement points and all investigated frequency bands, certain tendencies can still be observed. Specifically, patterns in wave propagation and level decay over distance and frequency emerge when analysing the spatial level decay L_a per distance, as well as the effective group velocity $c_{\mathrm{g,eff}}$.

5.1 Evaluation of a Local Versus a Global Behaviour of Structural Reverberation Time

There was noticeable variation in the reverberation times $\overline{T_{60}}$, both between measurement points and across third-octave bands at each point. Additionally, the mean reverberation times differed across all investigated frequency bands. Each measurement point is located within a complex geometry (a building), where the surrounding elements and transmission paths from the excitation point vary. These positional differences likely lead to distinct reflection patterns at each location.

The situation is further complicated by the unpredictable occurrence of modal peaks or wave interference, which can either enhance or suppress local reflections. Consequently, these effects influence the accuracy of local reverberation time measurements and make it challenging to generalise a single reverberation time for the entire structure.

The reverberation times obtained from the Comsol simulations appear more stable compared to the in-situ measurements. Although some variation across points and frequency bands remains, it is notably smaller. Furthermore, the simulated reverberation times are consistently lower than those measured in the real structure.

This discrepancy may be due to the Comsol model not fully capturing the actual boundary conditions or material properties of the building.

5.2 Exploration of the Proportionality Between Sound Level Decay per distance and the structural Reverberation Time

The findings presented in Tables 4.8 and 4.9 indicate that no clear proportionality exists between the reverberation time and the sound level decay with distance. The lack of proportionality may be attributed to uncertainties related to the modal behaviour of the structure, particularly whether the measurements sufficiently capture the contributions of both local and global modes present on the measured structure. While the results suggest a lack of proportionality, it remains unclear whether this is due to the absence of a true correlation or due to the influence of locally dominant modes acting within the structure. Therefore, no definite discussion can be had regarding a proportional relationship between sound level decay and structural reverberation time based on the current results. This is true for both the measurement and the simulation results.

A proportional relationship between the estimated group velocity $c_{\mathrm{g,eff}}$ for case 4 and the attenuation slope is observable for the results of both the measurements and the simulations, although the relationship is inverse. In the measurements, the effective group velocity decreases with increasing frequency, while in the simulations it increases. In the analytical fit model curves for case 4, higher frequencies tend to exhibit a more linear decay in level over distance, rather than a logarithmic one. Since the derivative of a linear function is constant, this would imply that the group velocity remains uniform over distance, which could explain the observed decrease in estimated velocity with increasing frequency in the measured data. If the Comsol data displays a more logarithmic decay at higher frequencies, this would correspond to an increasing group velocity with frequency, consistent with the trend observed in the simulations.

The observed increase in effective group velocity with distance was unexpected, as wave velocity is typically assumed to remain constant in a homogeneous medium such as concrete. A possible explanation may lie in the relative contribution of different wave types and their respective attenuation characteristics.

At frequencies above the critical frequency $f > f_c \approx 34\,\mathrm{Hz}$, longitudinal waves may begin to contribute more significantly to the energy transport. These waves propagate non-dispersively as shown for the velocity in Equation 2.10. In contrast, bending waves in plates are more strongly affected by both material damping and geometrical attenuation, leading to a more rapid decay of their amplitude with distance.

It is important to note that all investigated frequency bands in this study begin at 50 Hz, which is above the estimated f_c. This enables radiation into the surrounding medium and allows both geometrical spreading and relatively low damping factors (loss factors, η) to influence the behaviour of bending waves at these frequencies.

Consequently, at shorter distances, the measured response is likely dominated by the slower and more heavily attenuated bending waves. At greater distances, however, the contribution from longitudinal waves may become more prominent due to their higher propagation velocity and non-dispersive behaviour. This shift in dominant wave type could explain the apparent increase in effective group velocity with distance. In other words, the energy measured at longer ranges may increasingly reflect the presence of longitudinal components rather than bending waves.

When discussing the effects of geometric spreading and damping, the level decay observed between floors 3 and 5 suggests a geometric influence, particularly close to the excitation point, (see Figure 4.13 and 4.14). This behaviour aligns with the analytical curve fitting for Case 1, see Figure 4.3. At longer distances, the decay corresponds more closely with the analytical solution in Case 2, which includes only damping (Figure 4.5). This supports the idea that a reverberant energy field is only established beyond approximately 10 meters. At shorter distances, the reverberant-field assumption is not valid, as energy decay is dominated by direct propagation and geometrical effects.

When comparing the Comsol simulations with in-situ measurements for the vibration level decay across floors L_a over distance (see Figure 4.13 and Figure 4.14), it can be seen that the simulated results for floors 3 to 5 consistently yield lower vibration levels than the measurements across all investigated third-octave bands.

For positions close to the source, the difference between measured and simulated values varies from approximately 5 to 20 dB for all frequencies. At distances of 25 meters or more from the source. The simulated levels approach the measured values, typically reaching L_a levels between -10 and -30 dB.

This finding may indicate that the simulations for this study is better at representing the level decay behaviour L_a of the vibrations at longer distances. Whereas at shorter distances from the excitations point, additional unknown factors possibly not accounted for in the model might have a stronger influence on the vibrational level decay L_a per distance. However, the simulations thus appear to capture the general decay trend more reliably at greater distances, while deviations closer to the source may result from unmodelled effects, which may not have been considered in the simulations.

5.3 Time Delay and Its Use in Estimating Group Velocity

The positive trend in both the in-situ measurements and the Comsol simulations for the time delay as a function of all third octave bands supports the assumption that the bending waves propagate through the structure, with an increasing time delay

over distance, see Figure 4.11 and Figure 4.12. However, the calculated effective group velocity, $c_{g,eff}$, increases linearly with distance, based on the fitted trendlines see Figure 4.17 and Figure 4.21. This may indicate that different factors, such as geometrical spreading and damping-related attenuation, dominate the energy losses at different distance ranges. In particular, the influence of geometrical spreading may lead to an increase in the effective group velocity with distance.

This challenges the assumption of a constant group velocity, $c_{g,eff}$, and suggests that the structure does not exhibit a uniform reverberant field. The observed attenuation cannot be explained solely by damping. Instead, the increasing $c_{g,eff}$ points toward additional influences, such as geometrical spreading. Furthermore, early reflections may distort the impulse response close to the source, leading to underestimation of the local wave velocity and making $c_{g,eff}$ appear lower near the excitation point. The fitted trendlines yield coefficient of determination values of $R^2 > 0.5$, indicating that the linear behaviour of $c_{g,eff}$ is fairly well supported by the data. This reinforces the conclusion that cylindrical spreading has a significant impact on wave propagation, and that assuming only damping, implying constant velocity, is not sufficient to describe the system's behaviour.

5.4 Societal and Ethical Considerations and Need for Further Evaluation

The study on the vibrational behaviour of bending wave propagation in concrete buildings has provided some insights, but it still requires more data from in-situ measurements to better predict vibration levels in the early stages of housing development. As previously mentioned in Section 1.1, there is a significant concern regarding the negative effects of structural vibrations and the resulting airborne noise radiated from vibrating building elements. From an ethical standpoint, these findings are crucial when designing future buildings with mixed-use functions, particularly in cases where residential areas are located near businesses that generate high levels of vibration.

6
Conclusion

After investigating the bending wave behaviour of concrete slabs across multiple levels of a building, both in-situ and through simulations in Comsol, the research questions have been addressed based on the results and the subsequent discussion. However, the limited data from the in-situ measurements suggests that more comprehensive conclusions can only be drawn by gathering additional data on various concrete structures with different boundary conditions. This is important because these conditions may significantly affect the vibrational propagation through a building.

6.1 Findings

- Is it possible to find a connection between the time difference Δt and the distance d between a receiver point and a driving point? Is the velocity $c = \frac{d}{\Delta t}$?
  - It is possible to find a connection between the distance and the time difference between a receiver and the driving point. The velocity appears to increase with distance, and the $c = \frac{d}{\Delta t}$ appears valid both for measured data and Comsol data and with different methods of investigation.
- Is there a proportionality between the difference in sound level and the difference in distance (dB/m), and the reverberation time?
  - In this study, no proportionality was found between sound level difference and the reverberation time.
- Is there a global structural reverberation time, or does it vary with location or transmission path?
  - Observations from the discussion and results indicate that reverberation time in such a structure cannot be assumed to be global. Therefore, a single, representative reverberation time for the entire structure cannot be reliably defined for the measured data for this study.
- Is there a way to identify and measure the time delays $t_1, t_2, t_3, \ldots, t_n$ at different distances from the source (where $t = t_0$)?

  - The way of identifying and measuring the time delays was found to be possible by both measurements and simulations, this by using the deconvolution of a system response and the backward integrated impulse responses using the centre time of gravity method.

- To what extent can a representative modal response, based on mode shapes and modal superposition, be modelled and simulated to accurately represent the dynamic behaviour of a real building using Comsol Multiphysics?

  - There are indications that such an analysis is possible, but a full investigation was limited by computational constraints. Accurately modelling the real office building and all its structural connections in Comsol proved challenging due to long computational processing times.

6.2 Future Work

Time constraints during the thesis limited the scope of investigations. New findings confirmed through Comsol simulations and measurements showed that the effective group velocity is higher over longer distances. Future research should explore whether longitudinal and bending waves dominate at different distances in the structure. Future work could include investigations as proposed below:

- **Investigating different wavetypes:** Investigate the deformations in all three dimensions and investigate how the longitudinal waves may contribute to the structural response. This is interesting, as it opens the possibility of conducting a more detailed analysis that includes an assessment of energy directionality over distance, to determine whether the effective group velocity is related to energy dissipation.

- **Investigating other structural systems:**
  Future studies should investigate homogeneous concrete buildings with other types of boundary conditions to better understand the internal energy losses. These aspects are relevant for analysing the distance attenuation of structure-borne vibrations L_a, and for evaluating the validity of analytical assumptions such as purely geometrical spreading.

- **Further validation before practical use:** The study needs further validation before its results can be applied to prediction tools or theoretical applications. Future research should include more measurements using various methods and cover a wider range of distances and measurement points. Additionally, further investigation is needed to effectively apply Comsol simulations to real buildings, as there were challenges in aligning real-time results with the simulated model.

References

[1] M. S. Kerstin Persson Waye and M. Ögren, "Hälsopåverkan av lågfrekvent buller inomhus," Naturvårdsverket, Sahlgrenska Akademin, Göteborgs universitet, Tech. Rep. 3:2017, 2017, pp. 4–5. [Online]. Available: https://www.naturvardsverket.se/4ac694/contentassets/7ee907c0c71b4cd28066972361f857e2/halsopaverkan-lagfrekvent-buller-inomhus.pdf?utm_source=chatgpt.com.

[2] International Organization for Standardization, "Mechanical vibration and shock — evaluation of human exposure to whole-body vibration — part 1: General requirements," Geneva, Tech. Rep. ISO 2631-1, 1997, Accessed on: 26 May 2025.

[3] M. Barron, *Auditorium Acoustics and Architectural Design*, 2nd ed. Abingdon: Routledge, 2009.

[4] SIS, Swedish Institute for Standards, "Byggnadsakustik - ljudklassning av utrymmen i byggnader - bostäder," Stockholm, Tech. Rep. SS 25268:2023, 2023.

[5] J. Cheng, "Theory and measurement of low-frequency structure-borne sound in concrete buildings: Structural vibration analysis of a concrete floor," M.S. thesis, Division of Applied Acoustics. Chalmers University of Technology, Gothenburg, 2025 [Online]. DOI: http://hdl.handle.net/20.500.12380/309252.

[6] International Organization for Standardization, "Acoustics - measurement of room acoustic parameters - part 2: Reverberation time in ordinary rooms," Geneva, Tech. Rep. ISO 3382-2, 2008.

[7] L. Cremer, M. Heckl, and B. A. T. Petersson, *Structure-Borne Sound: Structural Vibrations and Sound Radiation at Audio Frequencies*, 3rd ed. Berlin: Springer, 2005. DOI: 10.1007/b137728.

[8] W. Kropp, *Propagation and radiation of structure-borne sound*, Technical Acoustics I, Division of Applied Acoustics, Gothenburg, 2015 [Ebook].

[9] F. Fahy and D. Thompson, *Fundamentals of Sound and Vibration*, 2nd ed. London: CRC Press, 2015. DOI: https://doi.org/10.1201/b18348.

[10] Júlio M. Montalvão e Silva and Nuno M. M. Maia, Ed., *Modal Analysis and Testing* (NATO Science Series E: Applied Sciences). Dordrecht: Springer, 1999 [Ebook], vol. 363. DOI: 10.1007/978-94-011-4503-9.

[11] Roy R. Craig Jr. and Andrew J. Kurdila, *Fundamentals of Structural Dynamics*, 2nd ed. Hoboken, NJ: John Wiley & Sons, 2006.

[12] COMSOL Inc. "The finite element method (fem)." (February. 21, 2017. [Online]), [Online]. Available: https://www.comsol.com/multiphysics/finite-element-method.

[13] COMSOL Inc. "Multiphysics modeling with comsol® software." ([Online]), [Online]. Available: https://www.comsol.com/multiphysics.

[14] COMSOL Inc. "Eigenfrequency analysis." (May. 8, 2018. [Online]), [Online]. Available: https://www.comsol.com/multiphysics/eigenfrequency-analysis.

[15] M. Müller-Trapet, "On the practical application of the impulse response measurement method with swept-sine signals in building acoustics," *Journal of the Acoustical Society of America*, vol. 148, no. 4, 1864–1878 [Online], 2020. DOI: 10.1121/10.0001916.

[16] J. G. Proakis and D. K. Manolakis, *Digital Signal Processing*, 4th ed. Harlow: Pearson, 2014, Pearson New International Edition.

[17] A. S. Rybakov, "Improvement of the accuracy of the time position estimation of the gravity center of an analog signal on the basis of discrete samples," *Automatic Control and Computer Sciences*, vol. 45, no. 6, 307–313 [Online], 2011. DOI: 10.3103/S0146411611060071.

[18] The MathWorks, Inc. "octaveFilterBank – octave and fractional-octave filter bank." Accessed on: 26 May 2025. (n.d. [Online]), [Online]. Available: https://se.mathworks.com/help/audio/ref/octavefilterbank-system-object.html.

[19] S. Abe, *Pattern Classification: Neuro-fuzzy Methods and Their Comparison*. London: Springer, 2001.

[20] Fonec & Co., A. H. Bjerke, and G. Eliassen, *Archived structural drawings – hovfaret 17, oslo (gnr. 31, bnr. 55)*, Oslo Bygningskontroll archive, Drawings dated 1959–1977; reviewed courtesy of Brekke & Strand AB, 1959.

[21] SIS, Swedish Institute for Standards, "Eurocode 2: Design of concrete structures — part 1-1: General rules and rules for buildings," Stockholm, Tech. Rep. SS-EN 1992-1-1:2005, 2005.

[22] "Pressure acoustics, frequency domain." Accessed on: 19 May 2025, COMSOL Inc. (n.d. [Online]), [Online]. Available: https://doc.comsol.com/5.5/doc/com.comsol.help.aco/aco_ug_pressure.05.101.html.

[23] Autodesk Inc. "Autodesk revit." Accessed on: 27 May 2025. (n.d. [Online]), [Online]. Available: https://www.autodesk.com/products/revit/overview.

[24] Bluebeam Inc. "Bluebeam revu." Accessed on: 27 May 2025. (n.d. [Online]), [Online]. Available: https://www.bluebeam.com.

[25] Opak AB, *Brannplan, etasje 3–4*, Version B, 2 Mar 2017, internal sketch from Brekke & Strand AB, 2017.

[26] J. Frost. “How to interpret r-squared in regression analysis.” Accessed on: 26 May 2025. (n.d. [Online]), [Online]. Available: https://statisticsbyjim.com/regression/interpret-r-squared-regression/.

[27] The MathWorks, Inc. “fminsearch – search for local minimum of unconstrained multivariable function.” Accessed on: 26 May 2025. (n.d. [Online]), [Online]. Available: https://se.mathworks.com/help/matlab/ref/fminsearch.html.

[28] The MathWorks, Inc. “fitlm – fit linear regression model.” Accessed on: 26 May 2025. (n.d.), [Online]. Available: https://se.mathworks.com/help/stats/fitlm.html.

A

Appendix

A.1 In-Situ

A.1.1 Reverberation time (T_{60}) at all measurement points, 50–160 Hz (in-situ) : Slabs and pillars

Calculated T_{60} for the slabs							
Point	**50 Hz**	**63 Hz**	**80 Hz**	**100 Hz**	**125 Hz**	**160 Hz**	**ΔL (m)**
M1	1.031	1.280	1.133	1.018	1.406	1.338	10
M2	2.011	1.515	1.268	1.136	0.453	0.671	4
M3	1.002	0.845	0.857	0.442	0.965	1.060	2
M4	0.990	0.857	0.614	1.618	0.514	1.157	5
M5	0.704	1.040	1.531	1.293	0.727	0.829	11
M6	0.816	0.663	0.598	0.821	1.433	0.577	9
M7	1.161	0.687	0.666	0.802	0.461	0.599	6
M8	1.345	1.286	0.901	1.135	0.405	2.298	14
M9	0.992	0.984	0.842	0.766	0.931	0.832	11
M10	1.514	1.182	1.080	0.926	0.645	1.700	4
M11	1.035	1.292	1.554	0.773	0.618	1.574	6
M12	0.965	0.799	0.684	1.388	0.666	0.930	11
M13	0.842	1.746	0.661	1.375	0.894	1.166	14
M14	1.563	1.556	1.411	1.617	0.811	1.560	24
M15	2.006	2.090	1.862	2.122	0.977	1.397	37
M18	0.987	0.689	0.975	1.903	1.198	2.106	40
T1	0.896	0.943	4.637	1.153	1.709	1.476	10
T2	1.050	1.001	2.467	0.683	1.095	1.159	8
T3	1.054	0.679	2.459	1.428	1.372	1.895	8
T4	1.116	0.830	1.212	1.152	0.774	1.209	13
T5	2.545	0.984	1.426	1.591	0.854	1.468	24
$\overline{T_{60}}$	**1.220**	**1.093**	**1.373**	**1.197**	**0.900**	**1.286**	(-)

Table A.1: T60 for each measured point on the floor/ceiling (slabs) for the measured data, with the averaged T_{60} for each third-octave band. The distance from the excitation point, ΔL is shown in the right-most column. To see the placement of each point, see Figure 3.6.

Calculated T_{60} for the Pillars							
Point	**50 Hz**	**60 Hz**	**80 Hz**	**100 Hz**	**125 Hz**	**160 Hz**	**ΔL (m)**
P1	1.005	0.977	0.505	0.990	0.528	0.801	9
P2	0.944	0.576	0.677	1.452	1.014	2.256	4
P3	0.782	0.468	0.543	1.286	0.439	1.072	4
P4	0.886	0.880	0.632	1.536	0.599	1.161	8
P5	0.585	0.645	0.445	1.457	0.575	0.567	12
P6	0.752	0.667	0.586	1.283	1.076	1.388	12
P7	0.837	0.624	0.705	1.629	1.231	1.486	8
P8	1.495	1.175	0.816	0.938	1.802	1.045	4
P9	1.070	0.660	1.486	1.457	1.408	0.809	4
P10	1.088	0.936	1.388	1.286	1.401	2.471	9
P11	0.630	0.945	0.670	0.664	0.658	1.184	37
P12	1.143	0.699	0.661	0.940	0.682	1.001	32
P13	0.873	0.896	0.597	1.422	1.105	1.671	27
P14	0.799	1.090	0.497	0.979	0.853	1.612	22
P15	1.604	3.789	1.608	1.457	0.681	1.309	18
P16	0.624	0.648	2.898	0.996	1.035	1.719	13
P17	0.771	0.924	3.730	1.881	1.052	1.288	13
P18	1.195	0.850	2.208	0.734	1.015	3.431	9
P19	1.142	0.709	2.723	1.658	0.879	1.942	5
P20	1.128	0.717	0.726	1.478	0.858	0.989	6
P21	5.062	0.967	1.320	1.256	1.029	1.182	6
P22	0.795	0.983	0.962	2.127	1.675	1.349	9
P23	0.502	0.782	0.750	0.947	0.375	2.043	10
$\overline{T_{60}}$	**1.118**	**0.940**	**1.180**	**1.298**	**0.955**	**1.469**	(-)

Table A.2: T60 for each measured point on the pillars for the measured data, with the averaged T_{60} for each third-octave band. The distance from the excitation point, ΔL is shown in the right-most column. To see the placement of each point see Figure 3.6.

A.1.2 Vibrational Level Over Distance for L_a Floor 3-5 (in-situ Measurement): Pillars

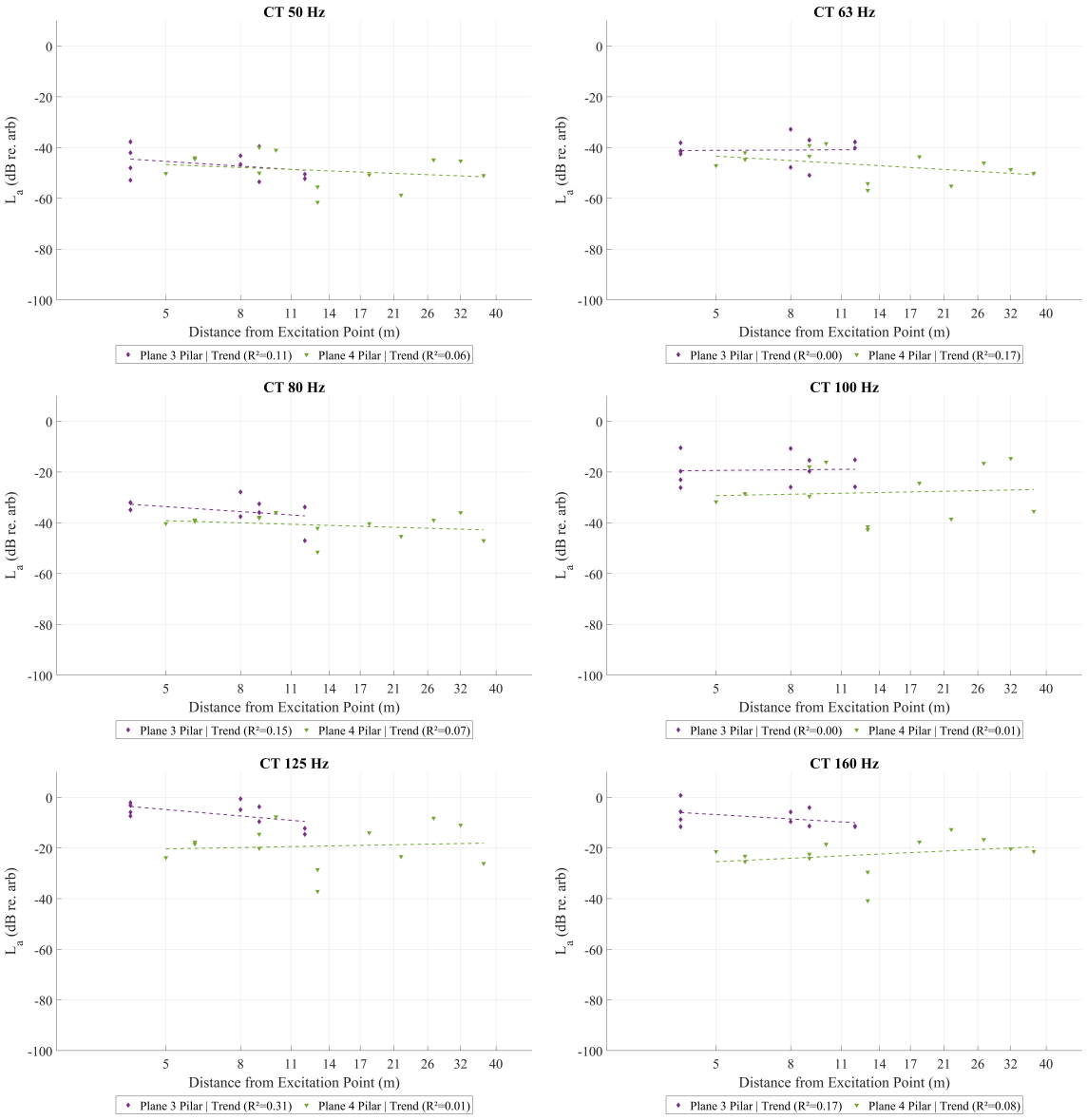

Figure A.1: The level attenuation for the measured pillar result. The dotted lines are fitted trends with their R^2-value. Top left to bottom right shows the third-octave bands 50 Hz to 160 Hz.

A.1.3 Spectogram for the Measuremnt Results

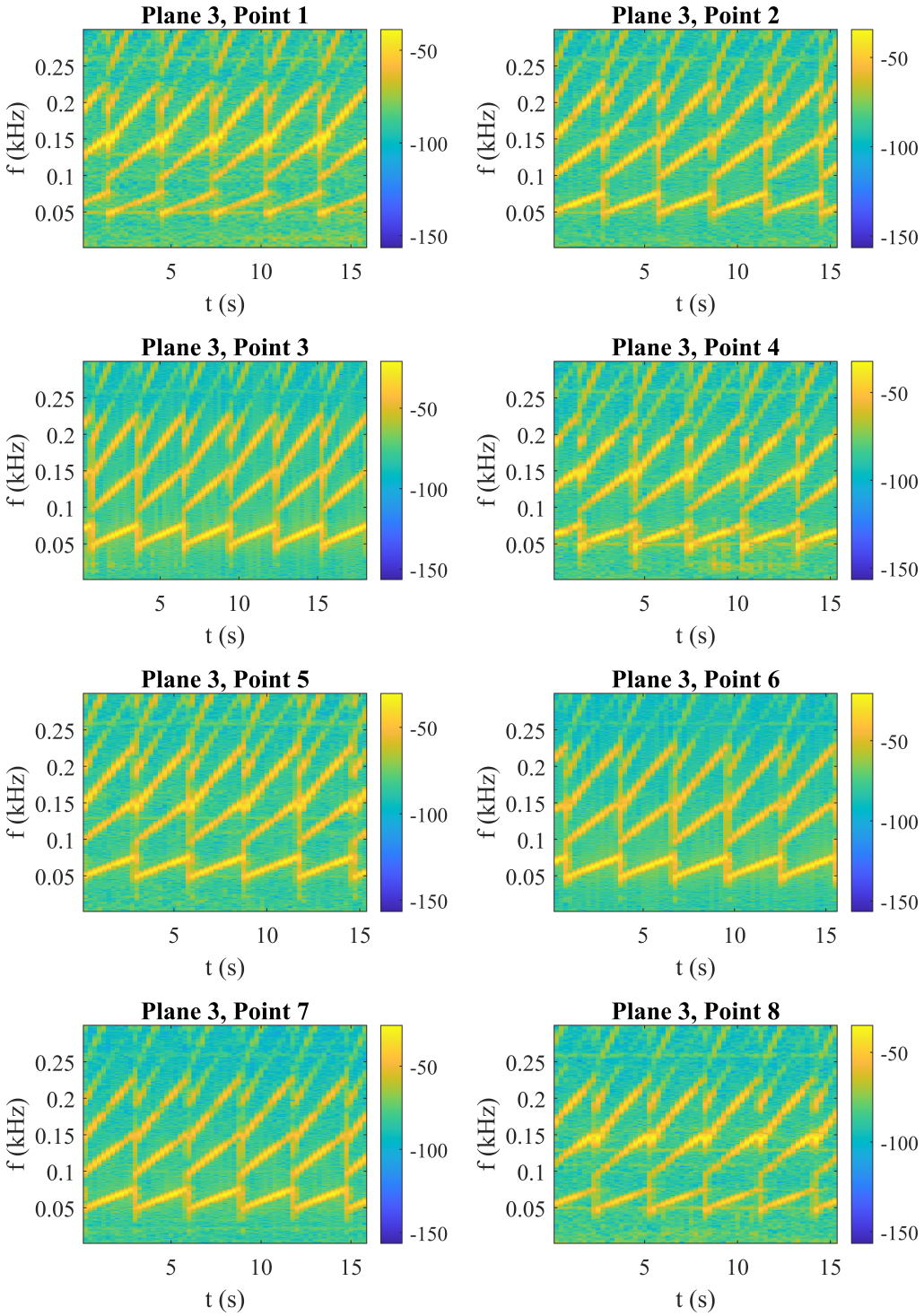

Figure A.2: The spectrograms of each measurement point for the slab on floor 3 in the in-situ office.

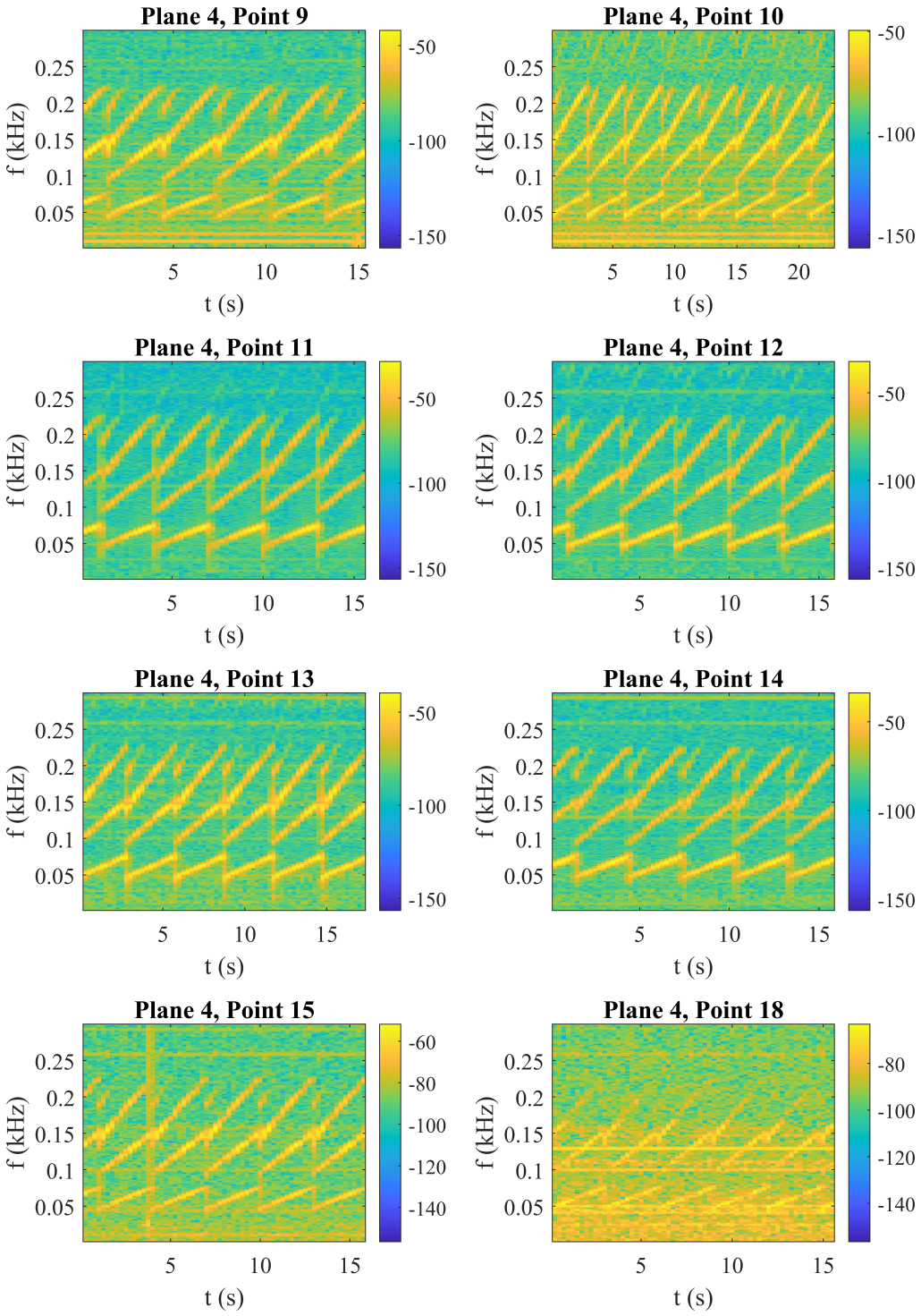

Figure A.3: The spectrograms of each measurement point for the slab on floor 4 in the in-situ office.

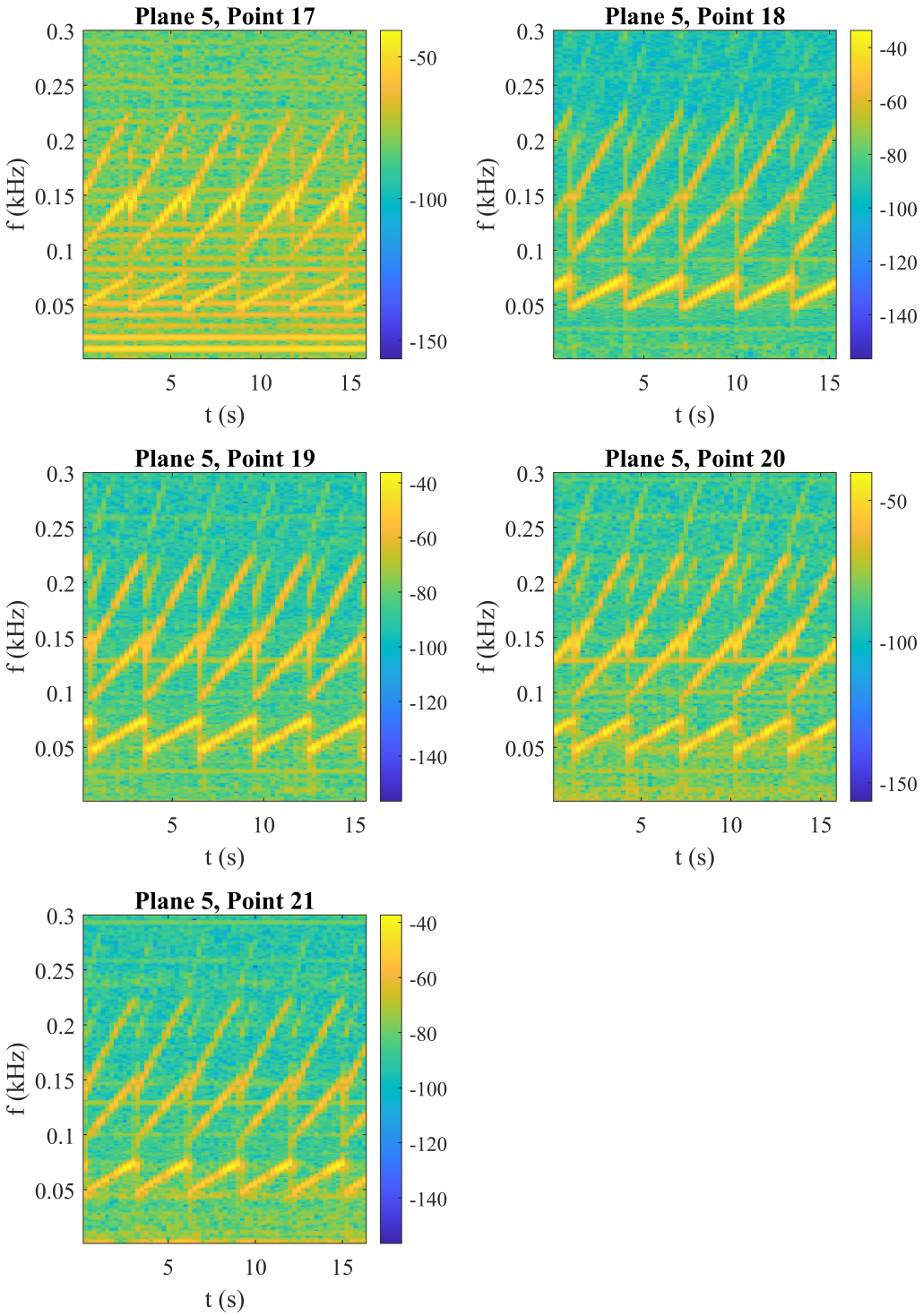

Figure A.4: The spectrograms of each measurement point for the slab on the roof i.e plane 5, in the in-situ office.

A.2 Comsol Simulations

A.2.1 Vibrational Level Over Distance for L_a Floor 3-5 (Comsol Simulation): Pillars

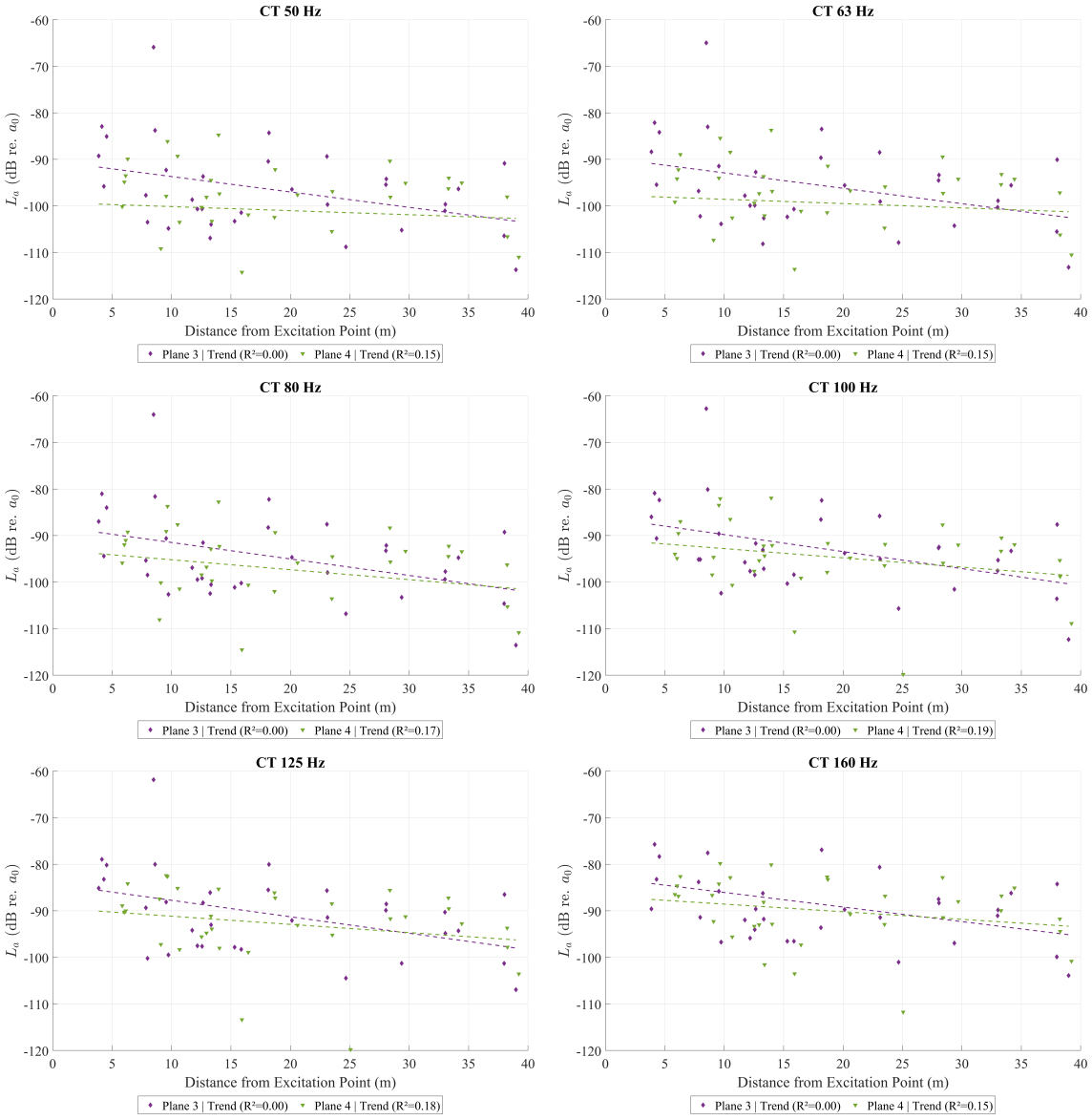

Figure A.5: The level attenuation for the measured slab result. The dotted lines are fitted trends with their R^2-value. Top left to bottom right shows the third-octave bands 50 Hz to 160 Hz.

DEPARTMENT OF SOME SUBJECT OR TECHNOLOGY
CHALMERS UNIVERSITY OF TECHNOLOGY
Gothenburg, Sweden
www.chalmers.se

CHALMERS
UNIVERSITY OF TECHNOLOGY